



Phase stabilisation, thermal expansion and ionic conductivity of high content rare earth oxide (Lu_2O_3 , Y_2O_3 and Gd_2O_3) stabilised cubic hafnia

Louise Sévin, Lisa Audouard, Volatiana Razafindramanana, Fabrice Mauvy, Leo Galzin, Jean-François Justin, Pierre Bertrand, Cécile Langlade, Garcia Matthieu, Aurélie Julian-Jankowiak

► To cite this version:

Louise Sévin, Lisa Audouard, Volatiana Razafindramanana, Fabrice Mauvy, Leo Galzin, et al.. Phase stabilisation, thermal expansion and ionic conductivity of high content rare earth oxide (Lu_2O_3 , Y_2O_3 and Gd_2O_3) stabilised cubic hafnia. *Journal of the European Ceramic Society*, 2023, 43 (9), pp.4153-4166. 10.1016/j.jeurceramsoc.2023.03.006 . hal-04064798

HAL Id: hal-04064798

<https://hal.science/hal-04064798>

Submitted on 7 Jul 2023

HAL is a multi-disciplinary open access archive for the deposit and dissemination of scientific research documents, whether they are published or not. The documents may come from teaching and research institutions in France or abroad, or from public or private research centers.

L'archive ouverte pluridisciplinaire **HAL**, est destinée au dépôt et à la diffusion de documents scientifiques de niveau recherche, publiés ou non, émanant des établissements d'enseignement et de recherche français ou étrangers, des laboratoires publics ou privés.

Phase stabilisation, thermal expansion and ionic conductivity of high content Rare Earth oxide (Lu_2O_3 , Y_2O_3 and Gd_2O_3) stabilised cubic hafnia

L. Sévin^{abc}, L. Audouard^{abc}, V. Razafindramanana^c, F. Mauvy^d, L. Galzin^d, J-F. Justin^a, P. Bertrand^b, C. Langlade^b, M. Garcia^c, **A. Julian-Jankowiak^{a,*}**

^a ONERA/DMAS-Université de Paris-Saclay, Châtillon, 92320 France

^b Université de Bourgogne Franche-Comté, laboratoire ICB UMR CNRS-UB-UTBM 6303, 90010 Belfort France

^c Direction des systèmes orbitaux, CNES, Toulouse, 31410, France

^d CNRS, Université de Bordeaux, ICMCB, UMR 5026, 87 Avenue du Dr. Albert Schweitzer, 33608 F Pessac Cedex, France

Abstract:

For satellite propulsion, new material are developed to sustain harsh thermal and environmental conditions in the combustion chambers induced by the development of new “green” propellants less toxic than currently used hydrazine. In the present study, hafnia-based materials with different amounts and natures of stabilisers (Lu_2O_3 , Y_2O_3 and Gd_2O_3) have been chosen for the ceramic part of the system. Microstructures, Thermal Expansion Coefficients (373-1673 K) and ionic conductivities (600-1273 K) of synthesised fully stabilised fluorite phases have been investigated. Lattice parameters have been determined and an abacus has been proposed as a function of the amount of RE_2O_3 and the ionic radius of the Rare Earth cation (RE^{3+}). Moreover, it has been observed a TECs decrease from 14 to 40 mol. % of RE_2O_3 and few changes in the ionic conductivity above 33 mol. % of RE_2O_3 . Finally, addition of Lu_2O_3 allows to reach the lowest TEC and ionic conductivity.

150 mots

Key words : Environmental Barrier Coating (EBC), HfO_2 , Rare Earth Oxide, Fluorite, ionic conductivity, Thermal Expansion Coefficient (TEC).

1 INTRODUCTION

Today, hydrazine propellant is commonly used for space propulsion. However, the European regulations are threatening the use of this monopropellant, which is considered as “substance of very high concern” because of its high toxicity and may ban its use in a near future. In this context, the need for new “green” propellant has become imperative for Europe to stay in the course of satellite propulsion and different solutions are studied [1–3]. Thus, CNES (National Centre for Space Studies) and ONERA (French Aerospace Lab) began to develop an alternative monopropellant with promising success in terms of energy efficiency and reduced toxicity. However this energetic compound has the drawback to develop harsh conditions which include a high temperature flame (> 2700 K) and very oxidising gases (particularly water vapour $\text{H}_2\text{O}(\text{g})$) [4]. Current solution of satellite thruster combustion chamber has been developed for 2000 K temperature flame application [5] and is composed of a refractory structural metallic component protected with a ceramic oxide as TBC. However, at higher temperature, the metallic layer cannot be used due to its melting point [6]. From there, to answer these requirements, CNES, ONERA and ICB-PMDM (French lab specialised in coatings) started research works focused on the development of new combustion chamber materials. Thus, a ceramic/metal Functionally Graded Material (FGM) has been designed and developed using Atmospheric Plasma Spraying (APS) [7]. In this context, the present study is centered on the development of a 2700 K resistant ceramic oxide layer as Environmental Barrier Coating / Thermal Barrier Coating (EBC/TBC). So, the aim of this work is to develop a highly refractory oxide ceramic having a low ionic conductivity to protect the metal part from oxidation and a thermal expansion coefficient fitting with that of an ultra-high refractory material support which has a quite low thermal expansion ($\sim 5\text{--}7 \cdot 10^{-6}$ /K).

In the literature, stabilised zirconia and more particularly, yttria partially stabilised zirconia (YPSZ) with a dopant concentration around 4 mol. %, are generally cited as TBC materials [8–14]. In more recent articles, new materials such as zirconia pyrochlore ordered phases [15–18] are studied due to their higher thermal stability, CMAS-resistance and thermal expansion which can match those of nickel-based superalloys with the adapted rare earth cations [19–21]. However, in the context of this study, these compositions based on zirconia do not fulfil the requirements of high reliability needed in space propulsion. Indeed, phase decomposition at high temperature for both compositions is among others the main failure in ultra-high temperature applications [22–24]. As hafnia (hafnium oxide, HfO_2) presents a very high melting point (3073 K), a low thermal conductivity [25] and a relatively low thermal expansion compared to others ceramics oxides [26,27], it seems to be one of the most promising candidates for thermal and environmental barriers in the context of this study. Also, some papers show the ability of hafnia based materials to be used as EBC as well as TBC for this type of application [11,25,28–32]. However, only a few studies have been carried out on its high temperature thermo-structural properties and generally, with limited information up to 2273 K [33].

Considering their similar crystalline structure and ionic radii of their cation 0.84 \AA (Zr^{4+}) and 0.83 \AA (Hf^{4+}) [34], zirconia and hafnia are considered as twin oxides. Moreover, they are both submitted to reversible allotropic phase transitions between the monoclinic (m), the tetragonal (t) and the cubic (c) systems [35]. Also, it is well known that the $m \rightleftharpoons t$ transition occurring during heating and cooling induces huge dimensional variations [36,37], which may be deleterious for the complete structure. Transition temperatures are reported as follow in the literature: 1973 K ($m \rightleftharpoons t$) and 2873 K ($t \rightleftharpoons c$) for hafnia [38] and at about 1443 K ($m \rightleftharpoons t$) and 2643 K ($t \rightleftharpoons c$) for zirconia [39]. Compared to zirconia, hafnia is a bit more refractory with a melting point higher of about 100 K, presents a higher $m \rightleftharpoons t$ transition temperature of about 600 K and exhibits a ionic conductivity twice as low as the one of zirconia systems [40]. Thus, it has been chosen to investigate hafnia instead of zirconia in the present study which concerns ultra-high temperature applications.

However, to reach phase stability up to 2700 K [37], the stabilisation of the cubic phase is mandatory as it eliminates the phase transitions that lead to cracks formation during cycling. Thus, trivalent rare earth oxide cations (Y^{3+} notably) are commonly used to stabilise zirconia or hafnia. As a consequence, to preserve the electro-neutrality of the structure, oxygen vacancies are created in the oxygen sub-lattice, generating an

oxygen deficient fluorite structure [34]. Also, Andrievskaya [22] and other authors [41–44] demonstrate that the melting point, the stability and the thermal expansion coefficient of the solid solution depend on the amount and the ionic radius of the stabilisers.

Regarding the amount of stabilisers, the stabilisation of zirconia with low content yttria has been widely studied in the literature [11,45–50], but only few studies deal with HfO₂-based materials [51–53]. Moreover, the use of high content of rare earth oxide for the stabilisation of hafnia is really not common in the literature and most of the papers deal with the stabilisation of hafnia with low yttria content (often around 8 mol. %) [54,55]. Very few studies concern higher amounts of stabiliser and are generally limited to 25 mol. % [32,56]. However, it has been proved that the amount of stabilisers has a significant influence on the material properties. As an example, increasing the amount of Y₂O₃ in HfO₂ leads to a decrease in thermal conductivity showing the interest of optimising the composition of HfO₂-Y₂O₃ ceramics to increase their performances for TBC applications [32]. As the performances of an EBC strongly depends on the oxygen diffusion resistance, ionic conductivity measurements have been carried out and reported in some studies. Thus, some authors, studying ceria and zirconia based materials, have shown that this property is also influenced by the concentration and the nature of the stabiliser [57,58]. For yttria stabilised zirconia with 8 mol. % of Y₂O₃ [59], a maximum in ionic conductivity is observed and a decrease for lower or higher doping rates. This phenomenon is directly related to a reorganisation process of the oxygen vacancies. In fact, few studies are dedicated to the ionic conductivity of HfO₂-based material as this property is generally investigated in the fuel cell research field with the aim to increase it as much as possible at the lowest temperature whereas it has been demonstrated that HfO₂ exhibits a largely lower ionic conductivity than ZrO₂ [40]. Furthermore, in our previous studies, hafnia based samples with different Y₂O₃ doping ratios have shown a high potential to fulfil the requirements of the present application. In particular, high amounts of additives (>33 mol. %) seem to be very promising [7,60,61] to reduce thermal expansion coefficient and ionic conductivity. Especially, ionic conductivity was reduced by two decades at 500 °C and one decade at 900 °C for HfO₂ monoliths containing between 12 and 33 mol. % of Y₂O₃ which could be potentially interesting in developments for environmental barrier coating applications (EBC). Thus, in the present paper, an increase in the amount of Y₂O₃ up to 50 mol. % is investigated to study the interest of very high stabiliser content.

Other studies have shown the influence of the ionic radius of the rare earth cation but few studies investigate HfO₂ based materials. As examples, Y₂O₃, Gd₂O₃ or Yb₂O₃ [51] but also Sm₂O₃, Dy₂O₃ [52] and Nd₂O₃, Er₂O₃ [53] in HfO₂ were studied but with low stabiliser contents. Fluorite systems composed of HfO₂ doped with Sc³⁺, Yb³⁺, Y³⁺, Tb³⁺, Gd³⁺ or Er³⁺ as solid solution with different host cation (Zr⁴⁺, Ce⁴⁺, Th⁴⁺, U⁴⁺) or pyrochlore systems [34,62–65] exhibit an increase in the ionic conductivity with smaller ionic radius. However, stabiliser amounts lower than 25 mol. % are considered in the studies. Moreover, considering the phases diagrams in the Andrievskaya's study, some rare earth oxides, as La₂O₃ or Nd₂O₃, involve a rapid decrease in the melting point of the HfO₂-RE₂O₃ solid solution when the amount of RE₂O₃ is increased [22]. Thus, in this study two other rare earth cations allowing the conservation of a very high melting point, Lu³⁺ and Gd³⁺, have been selected because they have very different ionic radii (0.977 Å and 1.053 Å, respectively). Moreover, compared to yttrium cation Y³⁺, they respectively present a lower and a higher ionic radius. Therefore, this study will give a better understanding of the influence of the rare earth ionic radius on the properties of the HfO₂-RE₂O₃ solid solutions with very high RE₂O₃ amounts (14-50 mol. %).

Such high amount of stabilisers are poorly described in the literature and will allow us to study the influence of the amount of RE₂O₃ and the ionic radius of RE³⁺ on both the thermal expansion coefficient (TEC) and the ionic conductivity of HfO₂-RE₂O₃ solid solutions.

Thus, in this paper hafnia samples with different additives as Lu₂O₃, Y₂O₃ and Gd₂O₃ in the range of 14 mol. % to 50 mol. % densified by natural sintering at very high temperature have been investigated. After the elaboration process, the microstructures of the samples have been characterised by Scanning Electron Microscopy and X-ray diffraction (XRD) to determine the grain size, homogeneity, porosity of the ceramic samples and lattice parameter. In addition, the chemical compositions have been estimated by Electron

Dispersive Spectroscopy and XRD. It should be noted that knowledge of these characteristics is crucial for further characterisations. Then, the coefficient of thermal expansion (473-1773 K) has been measured for each composition as well as the ionic conductivity. Thus, the relationship between the microstructure, the composition and these two studied properties as a function of the nature and the amount of rare earth oxide has been analysed.

These results will be useful to complete our understanding on the influence of additives on the stabilisation of hafnia.

2 EXPERIMENTAL PROCEDURE

In the present work, hafnium oxide or hafnia (HfO_2 , American Elements, $d_{50} \sim 0.1 \mu\text{m}$) has been stabilised in a fluorite cubic structure with three rare earth oxides (RE_2O_3): gadolinium oxide (Gd_2O_3 , Ampère Industrie, powder of purity $>99.9\%$, $d_{50} \sim 1 \mu\text{m}$), yttrium oxide (Y_2O_3 , American Elements, powder of purity $>99.9\%$, $d_{50} \sim 0.1 \mu\text{m}$) and lutetium oxide (Lu_2O_3 , Metall rare earth limited, nanosised powder). After drying overnight at 403 K, these powders were weighed to introduce 14, 20, 33, 40 and 50 mol. % of RE_2O_3 stabilisers in HfO_2 .

The powder mixtures were ball-milled for 4 hours in ethanol in a rotating mixer using zirconia media, dried in a rotating evaporator and shifted through a $50 \mu\text{m}$ sieve. In the case of high RE_2O_3 concentrations (≥ 33 mol. %), in order to initiate the solid solution formation before the sintering step, the mixtures were heat treated at 1823 K during 2 h in air. This stage has been added to avoid the presence of porosities and composition inhomogeneities in the final ceramics. Then, all the compositions were uniaxially pressed (20 mm in diameter) under a pressure of 50 MPa or pressed in a cold isostatic press (~ 20 mm in diameter) under 700 MPa during 2 min. After that, a three steps thermal treatment is carried out. First, a natural sintering step was performed on the pellets at 2023 K for 6 h under air. Then, depending on the composition and the attained microstructure, a second natural sintering step was performed at 2273 K for 2 h or 4 h under argon atmosphere in order to reach high densification levels ($>95\%$ of the theoretical density) and a similar microstructure between samples. Finally, the third step consists in re-oxidation of the pellets at 1173 K during 10 h under air to remove the oxygen vacancies created during thermal treatment under reducing condition. For very high amounts of RE_2O_3 (40 and 50 mol. %), another thermal treatment was also assessed. Indeed, only the first natural sintering step at 2023 K was performed for 6 or 8h under air as high densification rates were reached after this step contrary to the other RE_2O_3 contents. Thus, for these very high content of RE_2O_3 , both thermal treatments (at 2273 K and 2023 K) were assessed to study their influence on the material. All the materials and sintering conditions are listed in Table 1. For all the thermal treatments, a classical heating rate of $5^\circ\text{K}/\text{min}$ has been chosen and natural cooling applied.

The open porosities and apparent densities of all samples were measured by the Archimedes' method. Then, the densification level was calculated as the ratio of the apparent density to the theoretical density.

For each sample, X-ray diffraction was performed using an Empyrean PANalytical device (Bragg-Brentano configuration, θ - θ and Cu $K\alpha$ radiation) equipped with a linear X'Celerator detector. The diffraction range was from 10° to 110° with a 0.016° scanning step and 30 s counting time per step. Then phase identification and profile fitting were carried out with HighScore Plus 5.1 software using the full pattern Pawley method. A pseudo-Voigt peak shape with a split width and shape asymmetry type is used to model the peak profiles, while the Caglioti function describe the peak width (FWHM) [66]. The background is modelled using a 7-term Chebyshev type I function and the refined parameters are the specimen displacement, the lattice parameters, the Caglioti U, V and W variables and the peak shape 1, 2 and 3.

Thus, lattice parameters were determined from XRD patterns to calculate the theoretical density of the fluorite phase using the Ingel and Lewis formula [60]. Moreover, if secondary phases are detected through XRD, quantification is performed using the so-called "Direct Derivation (DD)" method proposed by H. Toraya

in 2018 [67], which is an option in the HighScore Plus 5.1 software. After that, these data can be introduced in the calculation of the theoretical density of the material using a mixture law.

Scanning Electron Microscopy (SEM, Mira Tescan) was used for microstructure examinations of the pellets surfaces after grinding with SiC paper and polishing with diamond naps down to 0.25 µm. The average grain size was determined by Electron BackScattered Diffraction (EBSD) with a SEM imaging (Merlin, Zeiss), after a meticulous polishing of the surface (by vibrating polishing with a colloidal silica suspension).

The average linear Thermal Expansion Coefficient (TEC) was determined under air flow (20 mL/min) from 373 to 1673 K with a heating rate of 5 K/min using a high-temperature dilatometer (SETARAM, SETSYS Evolution) over one to three cycles of heating, depending on the composition. Parallelepipedic ceramic sample dimensions were approximately 5x5 mm² and 10 mm in length.

Electrochemical Impedance Spectroscopy (EIS) measurements have been used to determine the ionic conductivity of the ceramics. During the experimental process, an alternative tension with variable frequency is applied between two electrodes. The signal amplitude varies between 10 and 200 mV and the frequency range between 1 Hz and 1 MHz. Impedance measurements allow the determination of the sample resistance and the ionic conductivity is then deductible with the following equation:

$$\sigma = \frac{1}{R} * \frac{e}{S}$$

Where R is the resistance of the sample (in Ω), e the thickness of the sample (in cm) and S the surface of the sample (in cm²).

In order to carry out these measurements, 15 mm in diameter and 1 mm thick discs (machined from sintered materials) were coated on their sides with a platinum ink and then fired at 1073 K for 10 h. All the measurements were performed under steady-state conditions in ambient air (PO₂=21.3 kPa) and over one cycle of heating and cooling between 600 and 1150 K.

*Table 1 : Theoretical density, apparent density and open porosity of the samples (*from measured lattice parameters and the Ingel and Lewis formula, \$ theoretical density calculated using a mixture law from XRD quantification)*

RE ₂ O ₃	RE ₂ O ₃ content (mol. %)	Reference	Sintering conditions	Theoretical density* (g/cm ³)	Apparent density (g/cm ³)	Open porosity (%)	Densification level (%)
Y₂O₃	14	Y-14	2273K-2h	9.157	8.859	0.00	96.75
	20	Y-20	2273K-4h	8.657	8.402	0.00	97.05
	33	Y-33	2273K-4h	7.704	7.610	0.51	98.78
	40	Y-40	2273K-4h	7.240	7.102	0.20	98.09
	40	Y-40b	2023K-6h	7.121 ^{\$}	6.827	0.84	95.95
	50	Y-50	2273K-4h	6.732	6.628	0.20	98.46
	50	Y-50b	2023K-6h	6.378 ^{\$}	6.526	0.10	100
Lu₂O₃	14	Lu-14	2273K-2h	10.298	9.929	0.44	96.42
	20	Lu-20	2273K-4h	10.224	9.867	0.46	96.51
	33	Lu-33	2273K-4h	10.037	9.694	0.50	96.58
	40	Lu-40	2273K-2h	9.850 ^{\$}	9.449	0.18	95.93
	40	Lu-40b	2023K-6h	9.900	9.421	0.08	95.16
	50	Lu-50	2273K-2h	9.664 ^{\$}	9.779	0.18	100
	50	Lu-50b	2023K-6h	9.687 ^{\$}	9.786	0.10	100
Gd₂O₃	14	Gd-14	2273K-2h	9.892	9.393	0.63	94.96
	40	Gd-40	2273K-2h	8.628 ^{\$}	8.343	0.15	96.70

40	Gd-40b	2023K-8h	8.668 ^s	8.501	4.66	98.10
50	Gd-50b	2023K-8h	8.484	8.071	2.06	95.13

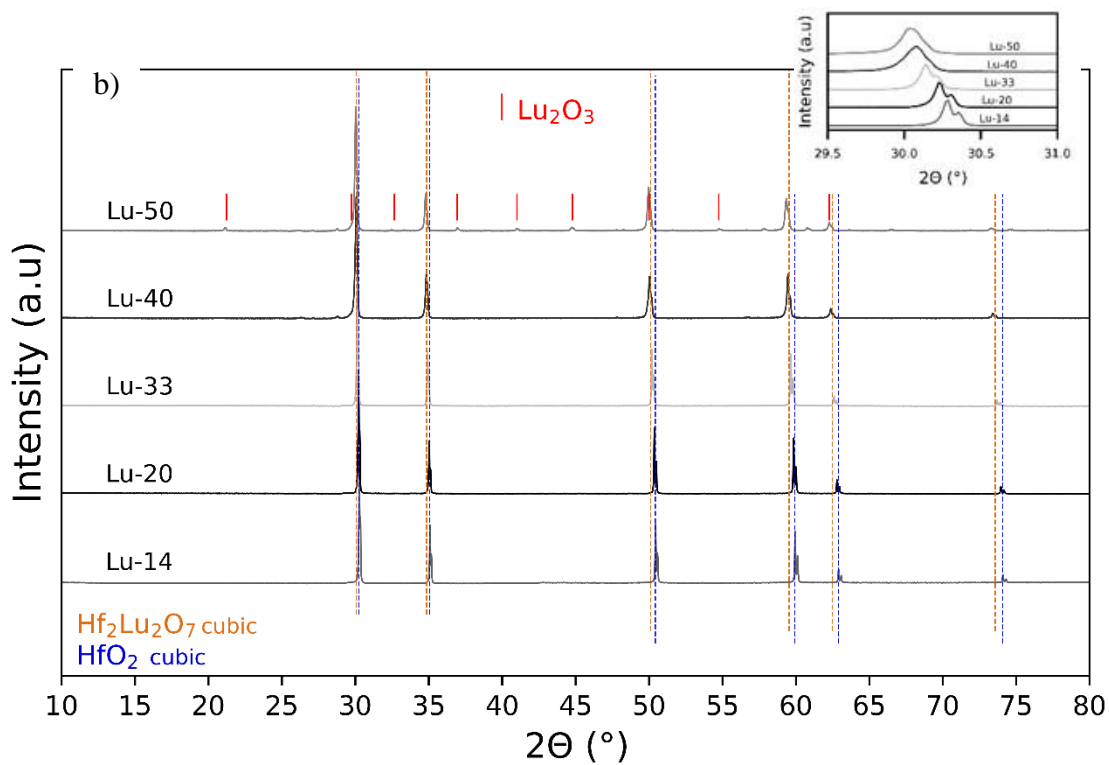
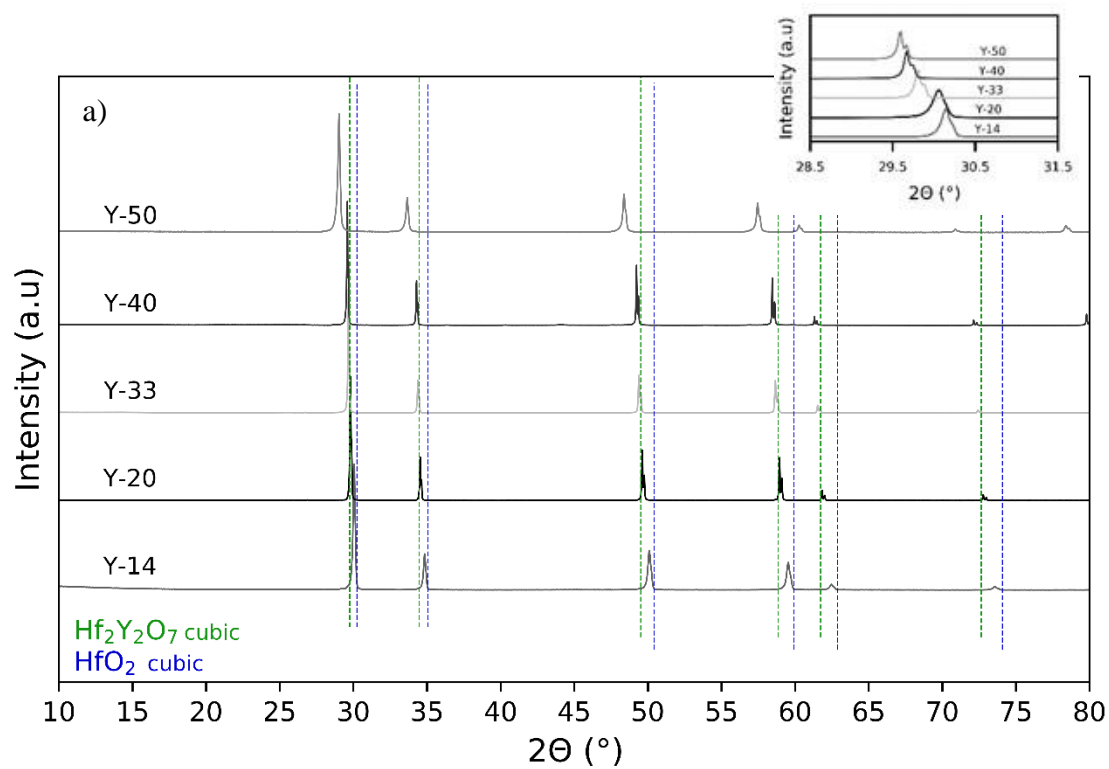
3 RESULTS AND DISCUSSION

3.1 Phase stabilisation

Before TEC and ionic conductivity measurements, the formation of the solid solution and the homogeneity of the samples have to be checked. The structural control was done using XRD and sample microstructure was examined by SEM examinations.

The XRD patterns of the solid solutions of $\text{HfO}_2\text{-Y}_2\text{O}_3$, $\text{HfO}_2\text{-Lu}_2\text{O}_3$ and $\text{HfO}_2\text{-Gd}_2\text{O}_3$ sintered at 2273 K as a function of the RE_2O_3 amount are presented in Figure 1. All the samples can be indexed with Fm-3m space group cubic structure with published data of a non-doped HfO_2 ideal cubic phase (JCPDS n°00-053-0560) and a disordered cubic phase called fluorite of following composition $\text{Hf}_2\text{RE}_2\text{O}_7$ (JCPDS n°00-024-1406, n°00-024-0425 and n°04-006-0133 respectively for $\text{Hf}_2\text{Y}_2\text{O}_7$, $\text{Hf}_2\text{Gd}_2\text{O}_7$ and $\text{Hf}_2\text{Lu}_2\text{O}_7$). In addition, as already mentioned in previous studies, the $\text{Hf}_2\text{RE}_2\text{O}_7$ phase is taken into account for the analysis of compositions with high concentration rates of RE_2O_3 (≥ 33 mol. %) [7,60]. For all patterns, neither the monoclinic phase nor the tetragonal phase have been detected in the XRD diagrams. Moreover, in the case of the studied cations, the empyrean criteria $r_{\text{RE}^{3+}}/r_{\text{Hf}^{4+}} < 1.46$ is always verified (lower than 1.26), thus the formation of the pyrochlore-type phase should be avoided [68–70]. It is verified for Lu^{3+} and Y^{3+} cations [70], however, a pyrochlore domain exists in the $\text{Gd}_2\text{O}_3\text{-HfO}_2$ pseudo-binary phase diagram [22]. Even if the selected amounts of Gd_2O_3 should allow to avoid this domain (40 mol. % is at the limit of the domain), the phase transition fluorite to pyrochlore could occur during the assessed heat treatments as it was observed by several authors [70,71]. They have shown that the transition from the fluorite to the pyrochlore structures proceeds via the emergence and the progressive growth of pyrochlore-type nanodomains in the fluorite matrix. In addition, in the case of Gd^{3+} cations, the reverse transition is possible during the cooling. The same composition is considered between the fluorite and the pyrochlore structures but anionic and cationic orderings are observed in the pyrochlore structures leading to an increase in the ionic conductivity. Thus, the formation of the pyrochlore structure should be avoided in our study.

After a sintering step at 2273 K, no secondary phases were detected in the cases of Y_2O_3 and Gd_2O_3 additions, whatever the RE_2O_3 concentration. For $\text{HfO}_2\text{-Lu}_2\text{O}_3$ materials, some characteristic peaks of the Lu_2O_3 phase have been observed for the Lu-50 material as it can be seen in the Figure 1. For $\text{HfO}_2\text{-Gd}_2\text{O}_3$ materials some characteristics peaks of the pyrochlore superstructure are only detected on the XRD diagrams of Gd-40 (JCPDS n°04-013-6940). This phase is not observed for lower and higher amounts as it is predicted by the phase diagram. The formation of this pyrochlore phase is allowed because of the low heating and cooling rates during the heat treatment. Some authors avoid the formation of this phase, quenching the material after heating [72]. The quantification of this phase is in the Table 2.



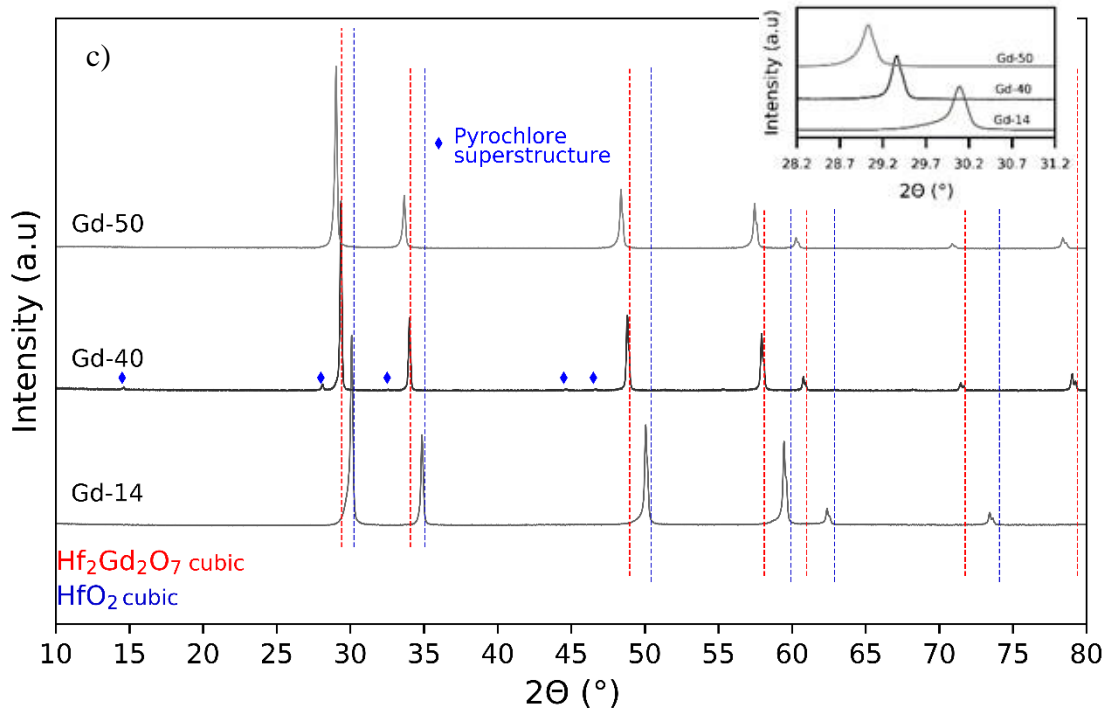


Figure 1 : XRD patterns of (a) HfO_2 -x mol. % Y_2O_3 (x = 14, 20, 33, 40 and 50), (b) HfO_2 -y mol. % Lu_2O_3 (y = 14, 20, 33, 40 and 50) and (c) HfO_2 -z mol. % Gd_2O_3 (z = 14, 40 and 50). Some characteristic peaks of the pyrochlore superstructure are indicated.

In the case of Lu-50, the amount of Lu_2O_3 is around 23 w. % using the Direct Derivation Quant Method of the software after the Pawley fit. The quality factor of the refinement (weighted profile residue: Rwp) is about 2 ($\ll 10$) indicating the good refinement. Examples of Pawley fits and quantifications are given in Figure 2 for Y-50b and Lu-40b sample.

After a sintering at 2023 K, RE_2O_3 have been still detected unless for Gd_2O_3 -based compositions and Lu-40b. However, Lu-40b XRD analysis reveals that formed phase is the rhombohedral $\text{Lu}_4\text{Hf}_3\text{O}_{12}$ phase (for 100 w. %) and not the expected $\text{Hf}_2\text{Lu}_2\text{O}_7$ fluorite phase (Figure 2) whereas in Lu-50b, the main phase is $\text{Hf}_2\text{Lu}_2\text{O}_7$ (for about 82 w. %). For this last sample, the amount of residual Lu_2O_3 is around 17 w. % and $\text{Lu}_4\text{Hf}_3\text{O}_{12}$ is also detected in very small quantity. The quantification results are reported in Table 2 and it is clearly seen that, the chemical compositions of Lu-50 (2273 K) and Lu-50b (2023 K) are very similar. Thus, increasing the sintering temperature for 50 mol. % of Lu_2O_3 does not lead to an increase of the quantity of $\text{Hf}_2\text{Lu}_2\text{O}_7$ which may be due to a limit of solubility of Lu_2O_3 in these conditions. Another point is that $\text{Lu}_4\text{Hf}_3\text{O}_{12}$ seems to be an intermediate phase in the chemical path to form the final fluorite $\text{Hf}_2\text{Lu}_2\text{O}_7$ phase as in the Yb_2O_3 - HfO_2 system [41]. As this phase is detected in very low quantity in Lu-50b, it can also be concluded that increasing the amount of Lu_2O_3 leads to a decrease in the temperature formation of the solid solution. In the case of Gd-40b, the pyrochlore structure is detected as in the case of Gd-40 because the transition temperature from the fluorite to the pyrochlore structures is exceeded in both thermal treatments. For higher amounts of Gd_2O_3 , the pyrochlore structure is not detected.

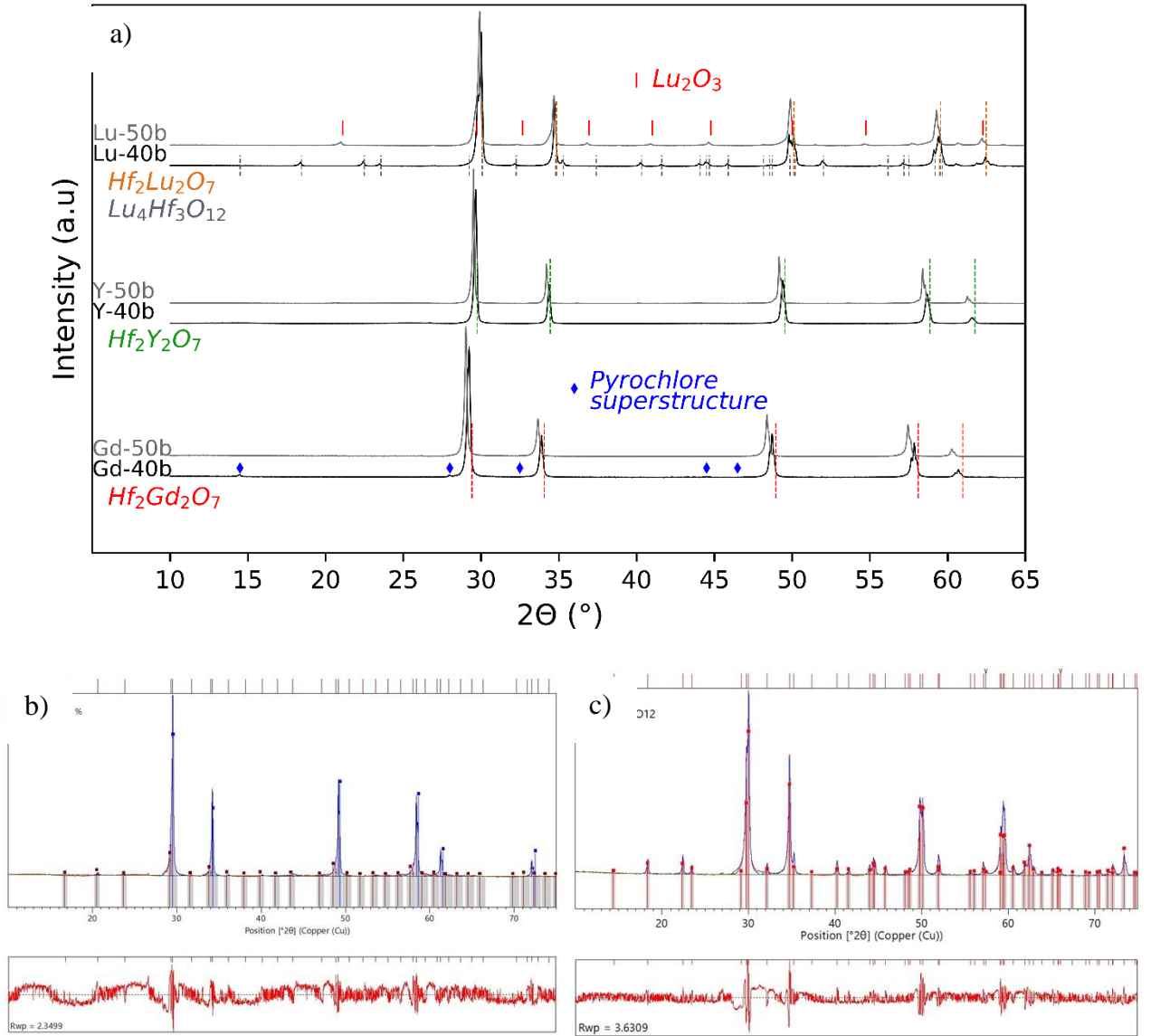


Figure 2: a) XRD analysis of all materials sintered at 2023K, b) Pawley fit and quantification results for Y-50b and c) Pawley fit and quantification results for Lu-40b.

Concerning the Y-40b and Y-50b, XRD refinements revealed the presence of the precursor Y₂O₃ after the sintering (2023 K - 6h) (Table 2) for about 4 w. % and 16 w. %, respectively. These proportions are consistent with the fact that Y₂O₃ have been introduced in excess in Y-50b compared to Y-40b. Indeed, the ideal proportion to obtain the stoichiometric Hf₂Y₂O₇ phase is Y-33.

As it has been seen before, the precursor Y₂O₃ disappeared after a final thermal treatment at 2273 K. Thus, the quantification results are summarised in Table 2.

Table 2 : Volume fractions of secondary phases in Y-40b, Y-50b, Lu-40b, Lu-50, Lu-50b, Gd-40 and Gd-40b from XRD analyses. (f is for fluorite and p for pyrochlore structures)

Samples	vol. % RE ₂ Hf ₂ O ₇ (f)	vol. % RE ₂ Hf ₂ O ₇ (p)	Vol. % RE ₂ O ₃	Vol % RE ₃ Hf ₄ O ₁₂
---------	--	--	---------------------------------------	---

Y-40b	94.6	0	5.4	0
Y-50b	79.2	0	20.8	0
Lu-40b	0	0	0	100
Lu-50	76.4	0	23.6	0
Lu-50b	81.8	0	17.2	1.1
Gd-40	39.5	60.5	0	0
Gd-40b	59.5	40.5	0	0

Then, the lattice parameters of all materials sintered at 2273 K were determined through Pawley refinements. Their evolution as a function of the RE_2O_3 content is reported in the Figure 3. For 50 mol. % Gd_2O_3 material, the lattice parameter has been calculated using a sample sintered at 2023 K. Nevertheless, as the fluorite solid solution is fully formed, it can be considered that the sample is fully representative. In the case of 40-Gd, as the pyrochlore and fluorite structures are detected in the sample, the lattice parameter of the fluorite structure is considered in the Figure 3. Few data are available in the literature regarding the lattice parameter of hafnia-based materials with high amount of RE_2O_3 . However, the present results for 14 mol. % of RE_2O_3 are in relatively good agreement with data from Trubelja et al. [73].

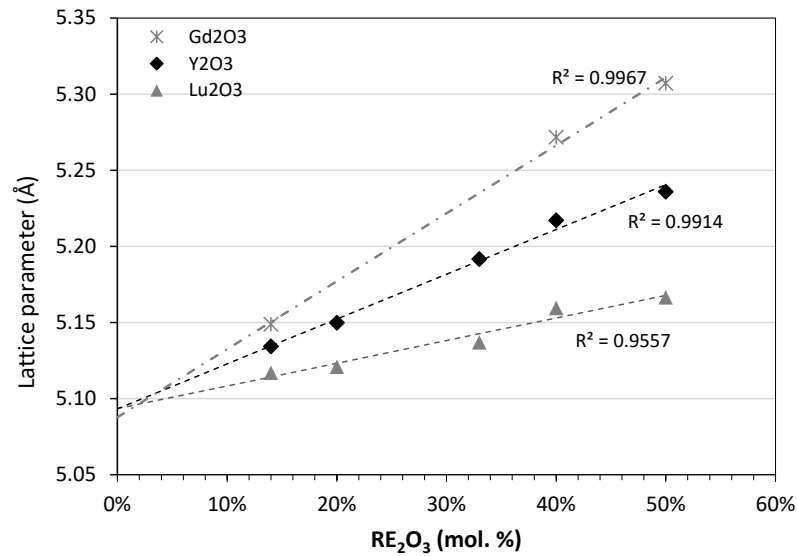


Figure 3 : Lattice parameters of the $\text{RE}_2\text{O}_3\text{-HfO}_2$ solid solutions as a function of the RE_2O_3 concentration ($\text{RE} = \text{Gd}, \text{Y}$ and Lu).

From the Figure 3, it can be noted that the lattice parameters are linearly correlated to the RE_2O_3 amount in the solid solution, thus a Vegard's type law (Eq 1) can be used to fit the data with good correlation rates (R^2) [74].

$$a = b \times x + c \quad (\text{Eq. 1})$$

Where a is the lattice parameter (Å), x the molar content of RE_2O_3 (%), b a constant depending on dopant species, and c the lattice parameter of the cubic hafnia without dopant (Å). For each RE_2O_3 studied in this paper, values for b and c are reported in the Table 3.

Table 3 : b and c values of the Vegard's law as a function of the rare earth oxide used.

RE_2O_3	b (Å)	c (Å)
Gd_2O_3	$4.46 \cdot 10^{-1}$	5.0878

Y₂O₃	2.94. 10 ⁻¹	5.0934
Lu₂O₃	1.49. 10 ⁻¹	5.0935

Based on the results from Figure 3 and using a linear regression, the predicted lattice parameter for a pure cubic HfO₂ without any addition of RE₂O₃ seems to be close to 5.09 Å. This is perfectly correlated with the JCPDS file for the cubic non-doped hafnia (a=5.095 Å) and other values from literature [75].

From these lattice parameters, theoretical densities of different compositions were calculated using the Ingel and Lewis formula [76]. The obtained values are reported in the Table 1.

To conclude the phase stabilisation part, fully formed fluorite Hf₂RE₂O₇ phases can be obtained by the solid state reaction at very high temperatures (2273 K). Lowering the sintering temperature to 2023 K induces in some cases the formation of an intermediate phase (Lu₄Hf₃O₁₂ in Lu-40b) or the presence of residual phases (*i.e.* RE₂O₃ in Y-40b, Y50-b and Lu-50b). In the case of materials with Gd₂O₃, the Hf₂Gd₂O₇ phase is fully formed at both temperatures and whatever the amount of rare earth oxide used, but the Hf₂Gd₂O₇ pyrochlore superstructure is detected for Gd-40 and Gd-40b. The lattice parameter evolves linearly with the amount of RE₂O₃ in the solid solution and the higher the ionic radius of RE³⁺ cation, the higher the lattice parameter.

3.2 Microstructures

After XRD analyses, the microstructures were finely characterised to determine the porosity level, the grain size and the homogeneity of the materials. The densification levels are superior to 95 % of the theoretical density (Table 1), thus all the samples are considered as fully dense.

3.2.1 Microstructures after sintering at 2273 K

Regarding materials with Y₂O₃, all the compositions are homogeneous whatever the amount of rare earth oxide (Figure 4) confirming the XRD analyses. Thus, it can be concluded that all the solid solutions are fully formed with a homogeneous composition. Moreover, the SEM examinations confirm the good densification levels of the samples (Figure 4).

The grain size is assessed through EBSD maps (for Y-14, 20 and 33) as this technique allows to take into account a large amount of grains [60]. The software Orientation Imaging Microscopy AnalysisTM was used to determine the grain size distribution in number. Several filters and hypotheses were applied such as excluding grains at the edge of the picture and modelling the grains as circles. Average grain size values are indicated on the micrographs (Figure 4) or reported in a previous study to be 15.6 µm and 20.2 µm for 20 mol. % and 33 mol. % of Y₂O₃, respectively [60]. Ytria-based samples exhibit an average grain size ranging from 13 to 20 µm, thus, microstructures are considered as equivalent.

The influence of RE³⁺ cations on microstructures is presented in Figure 4. The mean grain size was determined using the linear intercept method for the compositions with Lu₂O₃ and Gd₂O₃. For 14 mol. % of RE₂O₃, all the microstructures are homogeneous and similar with the same mean grain size (about 17-19 µm). When the amount of RE₂O₃ reaches 40 or 50 mol. %, grain growth is observed in solid solutions with Lu₂O₃ whereas the microstructure stays stable with others RE₂O₃.

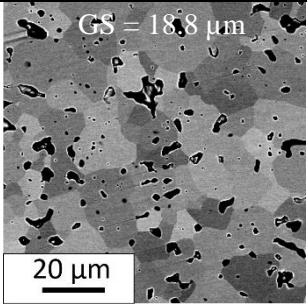
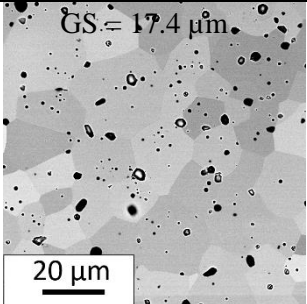
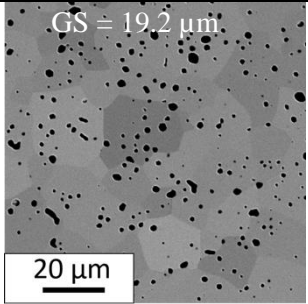
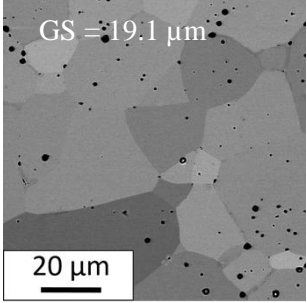
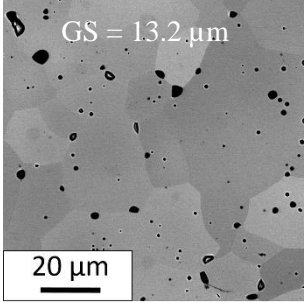
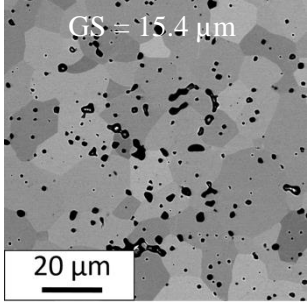
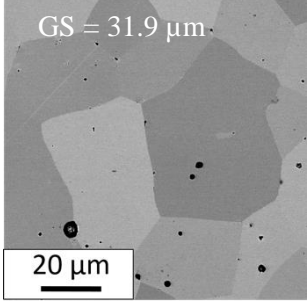
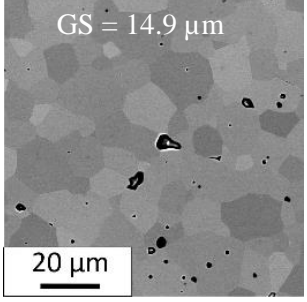
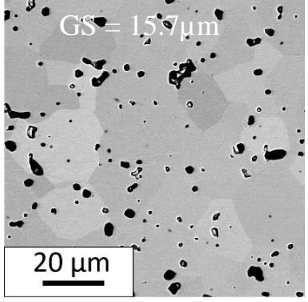
	Lu₂O₃	Y₂O₃	Gd₂O₃
14 mol. %			
40 mol. %			
50mol. %			

Figure 4 : SEM micrographs of HfO₂-RE₂O₃ solid solutions (RE= Gd, Y and Lu). GS is for the Grain Size determined through EBSD image analyses.

To conclude, microstructures are rather similar with a mean grain size ranging from 13 to 20 μm whatever the amount of RE₂O₃ and the nature of RE³⁺ except for Lu-50 for which there is a slight increase in the mean diameter (31.9 μm).

3.2.2 Microstructures after sintering at 2073 K

The microstructures of the materials sintered at 2073 K can be observed on SEM images reported in Figure 5. At fixed composition, the grain size seems to be much smaller than the same ceramic sintered at 2273 K. In addition, it can be mentioned that the grain size is always lower than 10 μm confirming that grain growth occurs during the last steps of the sintering process.

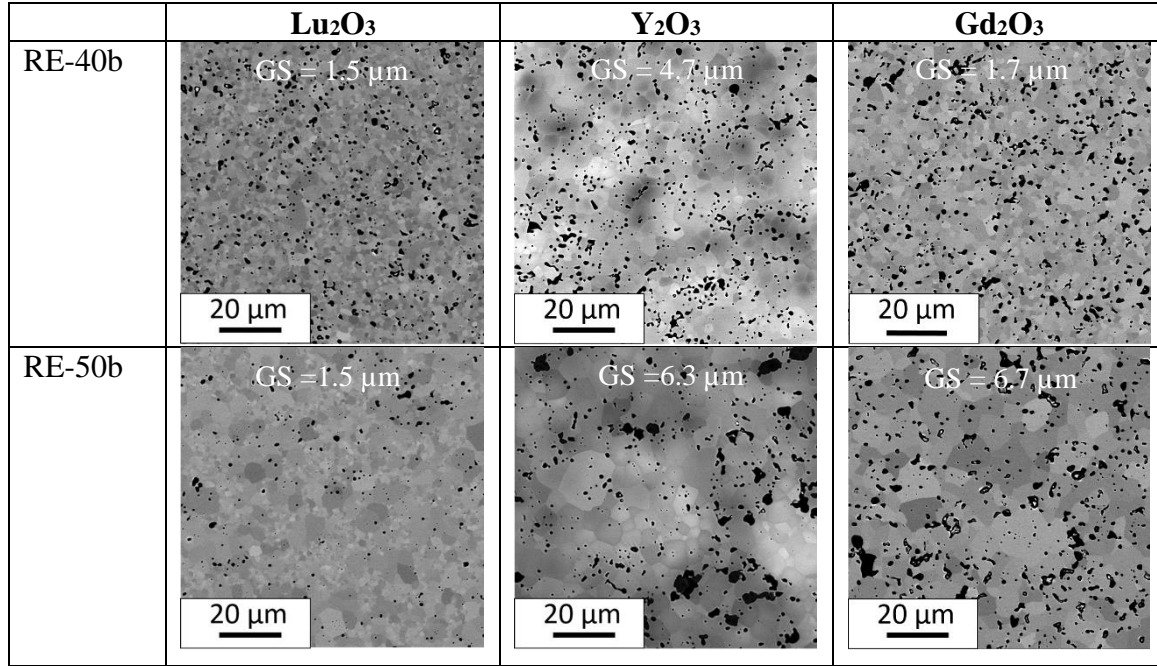


Figure 5 : SEM micrographs of $\text{HfO}_2\text{-RE}_2\text{O}_3$ solid solution with 40 and 50 mol. % of RE_2O_3 (RE= Gd, Y and Lu) sintered at 2023 K-6h (or 8h for Gd_2O_3 based materials). GS is for the Grain Size determined through EBSD images analyses.

3.3 Thermal expansion

Thermal expansion of the studied solid solutions has been measured under air and the thermal expansion coefficients (TEC) have been calculated as the slope between 473 and 1673 K.

3.3.1 Influence of the amount of Y_2O_3

Regarding solid solutions with Y_2O_3 sintered at 2273 K, the novel results are added to the previous one from [7] in the Figure 6. It can be noted that first the TEC decreases up to 40 mol. % of Y_2O_3 and then it increases again for 50 mol. %. Thus, the lower TEC is reached for the solid solution with 40 mol. % of Y_2O_3 .

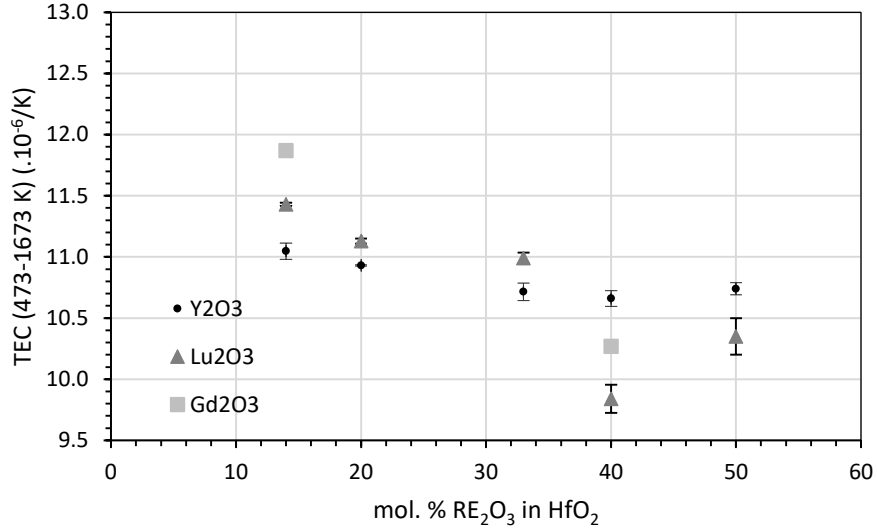


Figure 6 : TECs of $\text{HfO}_2\text{-RE}_2\text{O}_3$ solid solutions sintered at 2273 K ($\text{RE} = \text{Gd}, \text{Y}$ and Lu).

The thermal expansion of non-stoichiometric oxides with a fluorite structure similar to that presented in the paper by Marrochelli et al. [44,77] was studied and two phenomena were proposed to explain such variations: firstly, the larger ionic radius of RE^{3+} compared to Hf^{4+} and secondly, the lattice relaxation around oxygen vacancies.

In the literature, compared to this work, most of the authors studied low RE_2O_3 content (< 12 mol. %). Thus, HfO_2 is mostly stabilised in the tetragonal phase and an increase in the TEC correlated with the increase in the RE_2O_3 amount is described and explained through the difference of ionic radii between RE^{3+} and Hf^{4+} [78,79]. However, in this paper, solid solutions with higher amounts of RE_2O_3 have been explored and therefore a decrease in the TEC could be observed in the fluorite structures. Thus, the ionic radius cannot explain this trend and the second phenomenon should be taken into account. For this reason, the Born-Landé model has been used to explain the expansion phenomenon as a function of the RE_2O_3 amount and the nature of RE^{3+} . The Born-Landé equation (Eq. 3) considers the energy of the crystal lattice (U) which is inversely proportional to the dilatation.

$$U = \underbrace{\frac{N_A e^2}{4\pi\epsilon_0}}_{F1} M \underbrace{\left(1 - \frac{1}{n}\right)}_{F2} |Q^+||Q^-| \frac{1}{r_0} \propto \frac{1}{\alpha} \quad (\text{Eq. 3})$$

Where N_A is the Avogadro's number (in mol^{-1}), e the charge of an electron (in C), ϵ_0 the vacuum dielectric permittivity (in $\text{C}^2/\text{J.m}$), M the Mandelung's constant, n the Born exponent, Q^+ and Q^- the number of cationic and anionic charges, r_0 the distance between ions (in m) and α the thermal expansion coefficient (in K^{-1}). Moreover, F1 is a constant and F2 is calculated to be 2.519 for fluorite structures.

Considering equation 3 and an increase in the Y_2O_3 amount, thus Q^+ , Q^- and r_0 vary. Taking into account only Q^+ and Q^- , the TEC should increase with the amount of Y_2O_3 whereas the inverse is observed. Thus, r_0 seems to be the predominant factor governing the dilatation of the solid solution in the present case.

When introducing Y_2O_3 , oxygen vacancies are created according to the equation expressed in Kröger-Vink notation (Eq. 4):



These oxygen vacancies can generate several electrostatic interactions and some defect associations. From experiments and simulations, Marrochelli et al. have shown that removing an oxygen ion induces local distortions, which lead to a contraction of the lattice. Indeed, the creation of an oxygen vacancy resulting from the remove of an oxygen ion induces by the introduction of Y_2O_3 modifies the electrostatic interactions and especially anions are attracted closer to the vacancy as there is no more oxygen ion close to them. In the literature, several authors have shown that electrostatic interactions dominate around oxygen vacancies unlike steric ones [80,81]. Moreover, the vacancy radius due the oxygen vacancy is around 0.87 Å [44] which is largely lower than the oxygen ionic radius and the RE^{3+} radius (Table 4). This mechanism may explain the observed TEC decrease with the increase in Y_2O_3 content.

Furthermore, an increase in the TEC is observed when the amount of Y_2O_3 becomes higher than 40 mol %. This phenomenon can be explained by the fact that the number of Y-O bonds becomes higher than the one of Hf-O bonds. From Table 4, the binding energy of Y-O is lower than the Hf-O one. Consequently, increasing the amount of Y-O bonds leads to a global decrease of the lattice energy (decreasing r_0) and to an increase in the dilatation. Finally, taking into account a large range of stabilisers amount, the thermal expansion of the lattice first increases for amount of stabiliser lower than 12 mol. % as the ionic radius of RE^{3+} are higher than the one of Hf^{4+} [79,82,83]. However, above this amount of additives, a contraction of the lattice is observed as a consequence of the increase in the amount of oxygen vacancies [77]. Thus, these defects can reorganise in many ways to minimise the lattice energy, contracting the lattice. In the case of high RE_2O_3 amount (> 40 mol. %) the dilatation increases again as RE-O bonds are more numerous and weaker than Hf-O bonds.

Table 4 : Ionic radius, binding energy and atomic weight of studied ions.

	Hf⁴⁺	Lu³⁺	Y³⁺	Gd³⁺
Ionic radius (Å)	0.83	0.977	1.019	1.053
ΔH_{f(298)}(RE-O) (kJ/mol)	791±8	695±13	715±30	716±7
Atomic weight (g/mol)	178.49	174.97	88.91	157.30

3.3.2 Influence of the ionic radius

Regarding the influence of the ionic radius on the thermal expansion, the TEC of all the compositions sintered at 2273 K have been measured. The corresponding data are reported in the Figure 6. For solid solutions with Gd_2O_3 and Lu_2O_3 , the same evolution of the TEC than materials with Y_2O_3 is observed. Moreover, for 14 mol. % of RE_2O_3 , the solid solution with Y_2O_3 exhibits the lower TEC. These results show that the TEC is not directly linked to the RE^{3+} ionic radius as it was already observed for compositions with Y_2O_3 [44,60,77].

Considering only the influence of the ionic radius of RE^{3+} and a fixed amount of RE_2O_3 (14 mol.%), Q^+ and Q^- are equal for all the RE_2O_3 , thus, only r_0 varies in the Born-Landé equation (Eq 3). However, r_0 is not only correlated to the RE^{3+} ionic radius, it depends also on the charge of the system. Yashima et al. have studied the interactions and the bond length in the systems $\text{ZrO}_2-(\text{Y}-\text{Yb}-\text{Gd})_2\text{O}_3$ for a large range of RE_2O_3 in ZrO_2 (~0-40 mol. %) [81]. They have ranged the bond length as follow: $r(\text{Y}-\text{O}) < r(\text{Yb}-\text{O}) < r(\text{Gd}-\text{O})$. Taking in account that HfO_2 and ZrO_2 have very similar electronic structures and that Yb and Lu have almost the same ionic radius, the following classification can be considered: $r(\text{Y}-\text{O}) < r(\text{Lu}-\text{O}) < r(\text{Gd}-\text{O})$. This consideration could explain the TEC evolution as a function of RE^{3+} . The short bond length between Y^{3+} and O^{2-} could justified the low TEC reached with Y_2O_3 compared to the other RE_2O_3 . However, this mechanism is no more valid for high amounts of RE_2O_3 . Indeed, comparing Y_2O_3 , Lu_2O_3 and Gd_2O_3 -based systems, (Figure 6), the same trends have been observed with the TEC minimal value reached for 40 mol. %. The TECs measured for Lu-14, Lu-20 and Lu-33 are always slightly higher than the TEC for the same levels of incorporation of Y_2O_3 whereas the contrary has been observed for higher RE_2O_3 amount. Similar observations can be done for Gd-40 and Y-40 compositions. The TEC of Gd-40 is still lower than the one of Y-40. Thus, it seems that the influence of the bond length RE-O decreases with the increase of the amount of RE_2O_3 in the solid solution. The influence of the ionic radius of RE^{3+} becomes predominant over the bond length in the r_0 calculation. Another point that should be considered is that residual Lu_2O_3 is present in the Lu-50 material. As the TEC of Lu_2O_3 is lower ($7.7 \times 10^{-6} \text{ K}^{-1}$) [84] than the ones measured for $\text{Hf}_2\text{Lu}_2\text{O}_7$ so a decrease can be expected between Lu-40 and Lu-50. Thus, it is possible that the Lu-50 TEC could be higher without the presence of residual Lu_2O_3 . Considering Voigt and Reuss rules, and the amount of Lu_2O_3 quantified using XRD analyses (Table 2), thus the TEC of Lu-50 without secondary phase is estimated between 11.2 and $11.6 \times 10^{-6} \text{ K}^{-1}$.

3.3.3 Influence of thermal treatment

According to XRD analyses, it was deduced that the formation of $\text{RE}_2\text{Hf}_2\text{O}_7$ was not fully completed after a thermal treatment at 2023 K, therefore thermal expansion coefficients are compared for the samples Lu-40, Lu-40b, Lu-50 and Lu-50b in Table 5. Higher thermal expansion coefficients have been measured for materials sintered at 2023 K. The sample Lu-40b is mainly composed of the $\text{Lu}_4\text{Hf}_3\text{O}_{12}$ phase and its thermal expansion coefficient is a little bit higher than the one of Lu-40. Thus, it can be concluded that the formation of the $\text{Lu}_4\text{Hf}_3\text{O}_{12}$ phase does not lead to a decrease of the TEC.

Table 5 : Thermal expansion coefficients (473-1673 K) of Lu_2O_3 -based materials sintered at 2273 K (Lu-40 and Lu-50) and sintered at 2023 K (Lu-40b, and Lu-50b)

Thermal treatment	40 mol. % Lu_2O_3	50 mol. % Lu_2O_3
2273 K	$9.84 \times 10^{-6} \text{ K}^{-1}$	$10.35 \times 10^{-6} \text{ K}^{-1}$
2023 K	$10.54 \times 10^{-6} \text{ K}^{-1}$	$10.92 \times 10^{-6} \text{ K}^{-1}$

3.4 Ionic conductivity

As the ceramic layer of the developed combustion chamber material is both a Thermal and an Environmental Barrier coating, it should prevent the underneath layers from oxidation. In the present study, the oxidation of the underlying strata is mainly caused by the oxygen ion diffusion through the vacancies inside the ceramic layer. Indeed, due to the substitution of Hf^{4+} with RE^{3+} , oxygen vacancies are created to preserve the electroneutrality of the structure. As a consequence, an oxygen anions ionic conductivity can be induced according to a hopping model from one vacancy to another.

The ionic conductivity should follow an Arrhenius behaviour, which strongly depends on the temperature, as it is a thermally activated process as reported in equation 5:

$$\sigma T = A \times e^{\left(\frac{-Ea}{K_B T}\right)} \quad (\text{Equation 5})$$

Where T is the absolute temperature (K), Ea is the activation energy for conduction (eV), A is a pre-exponential factor (S.K/cm) and K_B is the Boltzmann constant (eV/K).

Thus, to study the influence of the RE_2O_3 nature and its amount on the diffusion mechanisms of oxygen ions through the electrolyte, several ionic conductivity measurements have been carried out for the studied compositions up to 1273 K.

The response of a sample to a sinusoidal alternative current with variable frequency generally leads to describe the sample as the parallel association of a Resistance and a Capacitance in which RC components correspond to the contribution from the bulk, grain boundaries and electrode/sample interface.

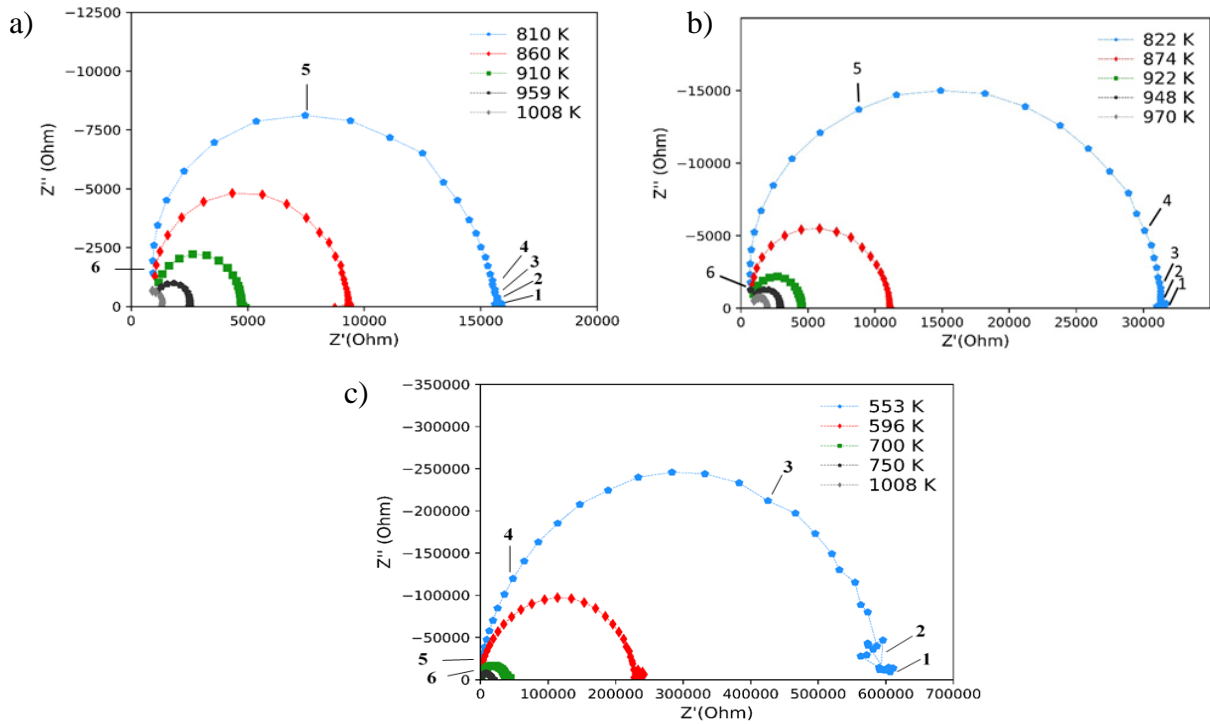


Figure 7: Impedance diagrams of a) the Pt/HfO₂-Gd₂O₃/Pt cell for Gd-50b, b) the Pt/HfO₂-Y₂O₃/Pt cell for Y-50 and c) the Pt/HfO₂-Lu₂O₃/Pt for Lu-50b measured at different temperatures (the numbers 1, 2, 3, 4, 5 and 6 indicated in the graphs are the logarithms of the frequency).

The evolution of the complex impedance diagram of Gd₂O₃, Y₂O₃ and Lu₂O₃-HfO₂ based systems as a function of the applied frequency is plotted on the Nyquist representation in Figure 7. As already observed in our previous study [60], only bulk resistivity is considered for the three systems considered in this study.

The part of the grain boundary is not detected in these measurements. It can be supposed that the resistivity of the grain boundary is too low to be detected or that the activation energy is the same for the bulk and the grain boundary because of a homogenous composition.

None of these hypotheses have been further analysed since the first purpose of the study is to assess the impact of the composition on the ionic conductivity and to confirm the measurement of bulk resistance.

3.4.1 Influence of the thermal treatment

The ionic conductivity measurements were performed on compositions with 40 and 50 mol. % Y_2O_3 sintered at 2023 K (Y-40b and Y-50b) and 2273 K (Y-40 and Y-50) to study the influence of the thermal treatment on oxygen transport properties. The ionic conductivity values as a function of the temperature are presented in Figure 8. The samples heat-treated at 2023 K show a little bit higher ionic conductivity. From Table 1, the porosity levels of the selected samples are very similar and cannot explain the observed differences. Also, the increase of the grain size with thermal treatment temperature could not cause the decrease of the ionic conductivity. Indeed, several authors shows that the grain boundaries act as diffusion barriers towards ionic species [85–87]. Thus, it can be due to the Y_2O_3 detected through XRD analyses. Indeed, the Y-40 and Y-50 samples are pure $\text{Y}_2\text{Hf}_2\text{O}_7$ fluorite structure phases whereas Y_2O_3 is still detected in Y-40b and Y-50b (Table 2). The Y-40b sample contains around 6 vol. % Y_2O_3 explaining the little difference in the ionic conductivity measurements between Y-40 and Y-40b. The difference between Y-50 and Y-50b samples seems larger and could be correlated to the higher amount of Y_2O_3 detected in Y-50b (~20 vol. %). Indeed, as there are some transitions areas around segregated areas of pure yttria, the diffusion of oxygen ions might be easier through these disordered areas compared to the oxygen deficient fluorite structure.

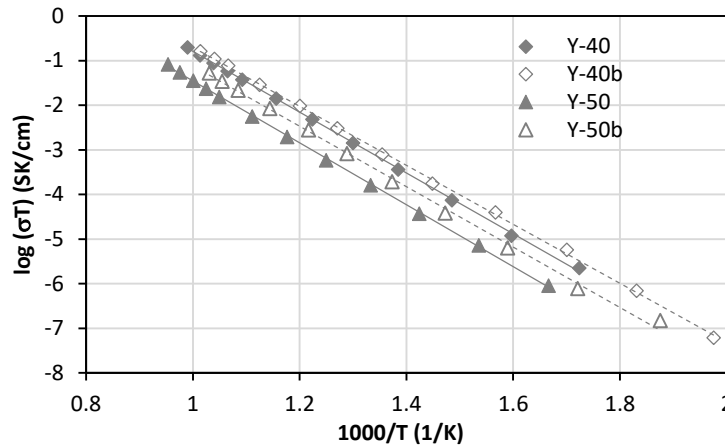


Figure 8 : Arrhenius plots for Y-40, Y-40b, Y-50 and Y-50b samples.

Thus, the presence of residual Y_2O_3 in the compositions Y-40b and Y-50b seems to explain their higher ionic conductivities compared to the pure fluorite sample.

3.4.2 Influence of the amount of RE_2O_3

Figure 9 represents the Arrhenius plots for different amounts of Y_2O_3 , Gd_2O_3 and Lu_2O_3 in the HfO_2 matrix. The accuracy of the Arrhenius law used to fit the ionic conductivity data as a thermally activated process is clearly demonstrated on these graphs.

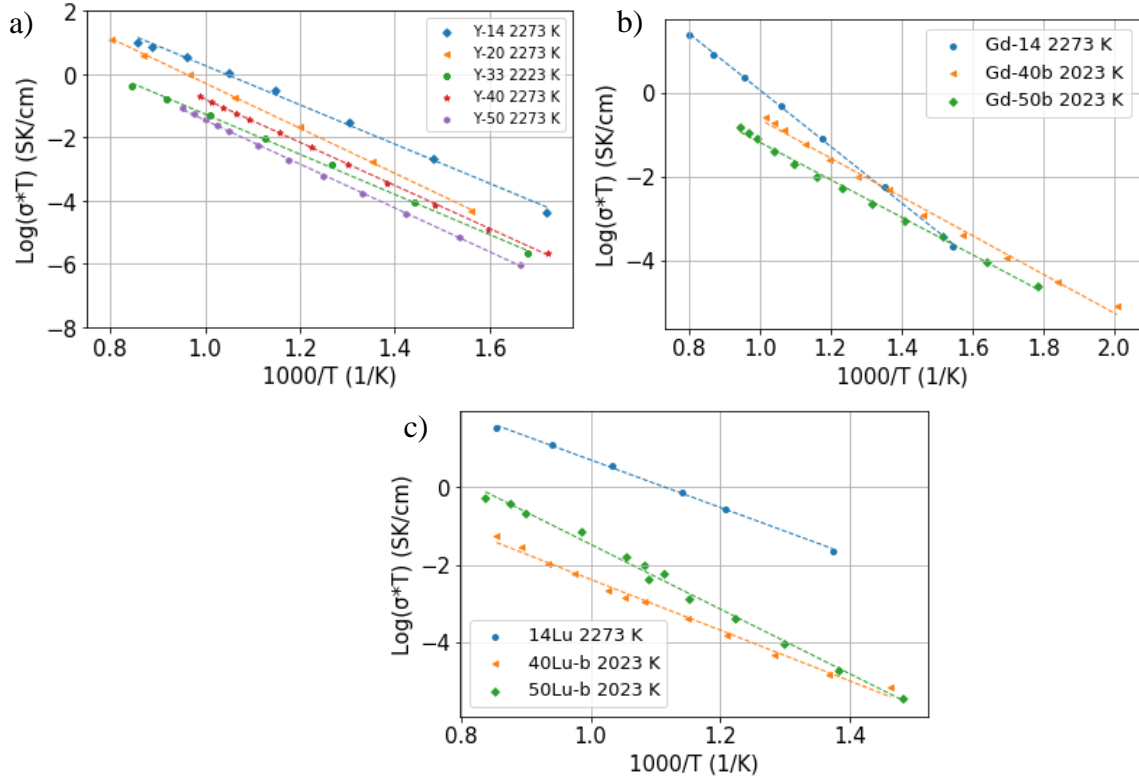


Figure 9 : Arrhenius plots for different amounts of (a) Y_2O_3 (b) Gd_2O_3 and (c) Lu_2O_3 in HfO_2

For Y_2O_3 -based compositions, all the studied samples presented on Figure 9(a) have been sintered at 2273 K. The increase of the amount of additive in hafnia induces a decrease in the ionic conductivity up to 50 mol. % except for Y-40 whose conductivity is between Y-20 and Y-33. In the case of Gd_2O_3 , Gd-14, Gd-40b and Gd-50b samples were studied as the samples are pure $Gd_2Hf_2O_7$. For these materials, a decrease of the ionic conductivity is measured up to 50 mol. % (Figure 9(b)). Concerning Lu_2O_3 -based materials, Lu-14, Lu-40b and Lu-50b were used for the ionic conductivity measurements. However, Lu-40b is mainly constituted of $Lu_4Hf_3O_{12}$ which should be considered in the interpretation of the results. In this case, a decrease of the ionic conductivity has been observed up to 40 mol. % and then an increase (Figure 9(c)).

The decrease of the ionic conductivity with the amount of RE_2O_3 up to 33 mol. % was already reported in our previous study [60]. Indeed, the introduction of higher amounts of additives induces a higher quantity of oxygen vacancies in the structure, thus leading to multiple defects arrangements. As oxygen ions move more easily through identical defects configurations, multiplying defect configurations leads to a decrease in ionic conductivity. Moreover, above a certain amount of additive, complexes between oxygen vacancies and cation RE^{3+} can be formed. These complexes decrease the mobility of the oxygen vacancies, which results in the diminution of the ionic conductivity [88]. More complex associations may occur with higher amounts of additive, so that they become neutral (in the case of the association of one oxygen vacancy with two cations) and could contribute to reduce the ionic conductivity [89].

For stabilised hafnia with trivalent cations, two types of oxygen vacancies may coexist at low temperature: the entities $RE'_{Hf}V_o^-$, which are vacancies associated to RE^{3+} cations, and the oxygen vacancies V_o^- which are free vacancies. The associated complexes $RE'_{Hf}V_o^-$, are the most probable type of existing oxygen vacancies as the position of RE'_{Hf} is randomly distributed. In the high temperatures range, the vacancies are considered as free only. Thus, the activation enthalpy for conductivity is the sum of the association/dissociation

enthalpy of the complex and the enthalpy of migration of the defaults, which can be expressed for trivalent additives by the following relation (Eq. 6):

$$H = H_m + H_a \quad (\text{Equation 6})$$

Where H_m is the migration enthalpy of the vacancies (in eV) and H_a the association enthalpy of the defects (in eV).

For yttria-based compositions, above 33 mol. % of yttria, the trend for ionic conductivity is not so clear. Indeed, it seems that above this ratio, which corresponds to the ideal proportion of yttria to form the disordered $Y_2Hf_2O_7$ phase, the incorporation of additional yttria induces other effects.

For low yttria content (12 and 14 mol. %) a small curvature is observed on the Arrhenius plots around 873 K whereas for high yttria content (20, 33, 40, 50 mol. %), the behaviour is more linear as it was already noticed in our previous study up to 33 mol. %. The small decrease of the slope between low and high temperatures (above 873 K) was previously explained by the difference of interactions between the defaults depending on the temperature [60]. Indeed, in the low temperatures range, defaults can be associated and interact whereas for the higher temperatures most of them are isolated and free.

Even if global enthalpy H is the addition of two contributions, especially for the lowest temperatures, H_a is the predominant one for the total activation enthalpy of the mechanism. This explanation is in good agreement with the fact that even if there is a decrease of the slope for low yttria content, this shift is very tiny. For the highest yttria concentrations, the amount of Y'_{Hf} is high enough to allow the formation of complexes even for the highest temperatures. Thus, for high yttria content, the total enthalpy is always the contribution of association and migration enthalpy whatever the temperature [90].

The calculated activation energies are reported in Table 6. For Y_2O_3 -based materials, considering only one slope, the highest activation energy is obtained for Y-20 with 1.42 eV. Moreover, two different activation energies were also calculated considering the transition temperature at 870 K. Regarding the Table 6, the low temperature activation energies are quite similar for all the Y_2O_3 -based materials ranging between 1.30 and 1.35 eV except for Y-20 (1.47 eV). These results confirm the previous observations indicating that, at low temperature, the Y_2O_3 concentration has no influence on the activation energy [60]. In contrast, at high temperature, the activation energy increases slowly with the amount of Y_2O_3 . Moreover, above 14 mol. % of Y_2O_3 , the low and high temperature activation energies are very close confirming the linear behaviour observed on the curves. It was proposed that at a high amount of Y_2O_3 , the defects interactions are stronger and a temperature of 1273 K is too low to reach their dissociation/disorder state. The decrease of the ionic conductivity at very high amount of Y_2O_3 can be explained by the increase in the level of substitution of Hf^{4+} by Y^{3+} . Indeed, several authors have shown that the preferential pathway for oxygen diffusion in doped zirconia is Zr-Zr edge rather than Zr-Y or Y-Y edges due to a lower activation barrier (0.5 eV, 0.9-1.3 eV and 1.3-2.0 eV respectively) [91,92]. Moreover, Zhang et al. have demonstrated using DFT calculations that ZrO_2 and HfO_2 have a similar electronic behaviour, thus the same order of magnitude is verified in HfO_2 . Hence, the probability for the O ion to pass across Hf-Y and Y-Y edges is much smaller. Thus, increasing the amount of Y-Y and Hf-Y bonds leads to a decrease in ionic conductivity. Moreover, it was found that an higher migration enthalpy is necessary for the diffusion of oxygen ions considering higher amounts of yttrium in zirconia [93].

Table 6 : Activation energy at low and high temperatures.

		Y-14	Y-20	Y-33	Y-40	Y-50	Y-40b	Y-50b	Lu-14	Lu-40b	Lu-50b	Gd-14	Gd-40b	Gd-50b
Ea (eV) 1 slope		1.23	1.42	1.26	1.35	1.31	1.38	1.34	1.11	1.30	1.65	1.29	0.98	0.89
Ea (eV) (2 slopes)	580-870 K	1.33	1.47	1.33	1.35	1.30	1.34	1.31	1.45	1.13	1.56	1.39	0.91	0.84
	870-1300 K	0.98	1.38	1.17	1.38	1.35	1.46	1.39	1.11	1.53	1.51	1.29	1.12	1.16

association energy (eV)	0.35	0.10	0.16	0.33	0.10
migration energy (eV)	0.98	1.38	1.17	1.11	1.29

Regarding Lu_2O_3 -based materials, Lu-50b exhibits a higher ionic conductivity than Lu-40b with a higher activation energy which could be explained by the differences in composition. Indeed, Lu-50b is mainly composed of $\text{Lu}_2\text{Hf}_2\text{O}_7$ with 17 w. % of Lu_2O_3 whereas Lu-40b is composed of $\text{Lu}_4\text{Hf}_3\text{O}_{12}$. The residual rare earth oxide phase shown an increasing of ionic conductivity for Y-40b and Y-50b samples (Figure 8). For these materials, if one slope is considered, increasing the amount of Lu_2O_3 leads to an increase in the activation energy. In Figure 9(c), a small curvature is observed for Lu-14 and Lu-50b with a decrease of the slope at high temperature. As for Y_2O_3 , the amount of Lu_2O_3 has no influence on the low temperature activation energy comparing Lu-14 and Lu-50b. At high temperature, the activation energy decreases significantly in the case of Lu-14 and remains almost constant for Lu-50b. Thus, the same explanations as for Y_2O_3 -based materials could be considered. At low content of Lu_2O_3 , the disorder/dissociation state is reached at high temperature (> 873 K). In the same way, H_a and H_m were calculated for Lu-14 only. In the case of Lu-50b the dissociation state is not reached at high temperature and H_a and H_m should be still considered in the activation energy. Moreover, from these results, it can be concluded that the rhombohedral phase has a much lower ionic conductivity.

Regarding Gd_2O_3 -based materials, unlike the two others RE_2O_3 , a small curvature is observed on the Arrhenius plots but with an increase in the slope at high temperature (Figure 9(b)). Moreover, the low temperature activation energy decreases when the amount of Gd_2O_3 increases and is lower than the one at high temperature, which is the contrary of the previous observations. Thus, materials with Gd_2O_3 have a very different behaviour.

3.4.3 Influence of RE^{3+} ionic radius

The ionic conductivities for RE-14 and RE-50 samples are reported in Figure 10. The results are comparable to the work carried out by Trubelja et al. [73] with 14 mol. % of RE_2O_3 .

Comparing Lu-14, Y-14 and Gd-14, the ionic conductivity increases when the ionic radius of RE^{3+} decreases. Moreover, the association enthalpies (Table 6) exhibit the following ranking: $H_a(\text{Gd-14}) < H_a(\text{Lu-14}) < H_a(\text{Y-14})$ with a very small difference between $H_a(\text{Lu-14})$ and $H_a(\text{Y-14})$. The migration enthalpies can be classified: $H_m(\text{Y-14}) < H_m(\text{Lu-14}) < H_m(\text{Gd-14})$. Comparing RE-50 materials, Lu-50 exhibit the lowest conductivity and Gd-50 the highest and the activation energies have the same ranking.

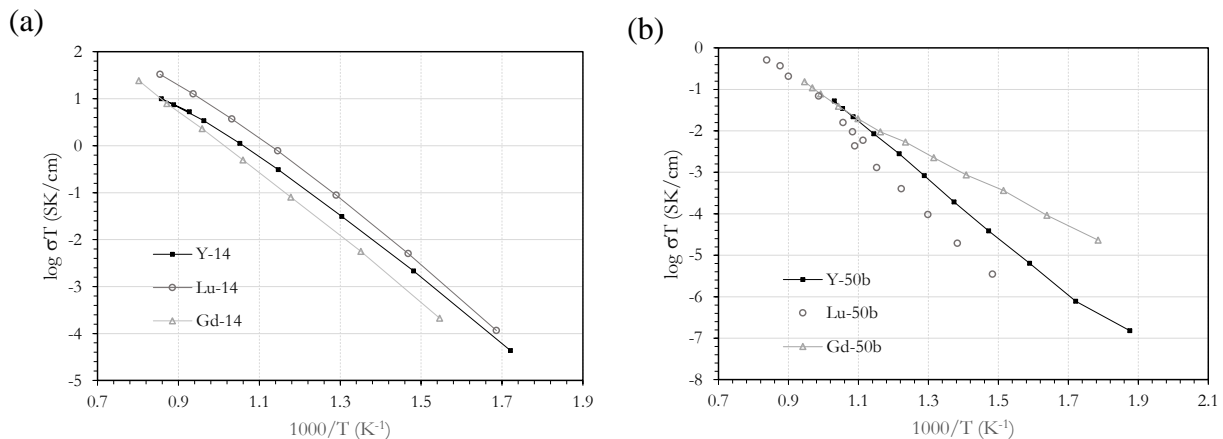


Figure 10 : Representation of the ionic conductivity for different temperatures considering (a) 14 mol. % and (b) 50 mol. % of Gd_2O_3 , Y_2O_3 and Lu_2O_3 in HfO_2

The association enthalpy H_a of the defects depends on several factors and strongly on the difference of the ionic radii between Hf^{4+} and RE^{3+} [88] or more precisely between the ionic radii of RE^{3+} and the ionic radii for which the lattice neither contract nor expand [94]. For trivalent cations and considering the ionic radii of Hf^{4+} , which is 0.83 Å, the size for which the lattice neither contract nor expand is around 0.94 Å. Moreover, from Trubelja et al. the association enthalpy depends on the r_{RE}/r_{Hf} ratio and reaches a minimal value when $r_{RE} = r_{Hf}$ [73]. They also mention that the dependence upon this ratio is much greater when r_{RE} is lower than r_{Hf} than when r_{RE} is higher than r_{Hf} . In the present study, all the host cations have a higher ionic radius than the one of Hf^{4+} . However, small amounts of RE_2O_3 are mentioned (<14 mol. %) in their study. Arachi et al. have shown for ZrO_2 - RE_2O_3 solid solutions with content of RE_2O_3 up to 15 mol. % that the enthalpy of association increases when the ionic radius of RE^{3+} decreases whereas the opposite is observed for the migration enthalpy [95]. Thus, as ionic radii of Lu^{3+} , Y^{3+} and Gd^{3+} are respectively 0.977 Å, 1.019 Å and 1.053 Å, H_a should be ranked as follow: $H_a(Lu-14) > H_a(Y-14) > H_a(Gd-14)$. In the present study, this ranking is not checked as H_a should be the highest for Lu-14 and not for Y-14. The same remark could be done for H_m as Lu-14 should exhibit the lowest value.

Another point to mention is that Butler et al. [96] have calculated the binding energy of associates (i.e. H_a) in ZrO_2 and found 0.28 eV for $Y'_{Hf}V_o^{\bullet}$ and 0.17 eV for $Gd'_{Hf}V_o^{\bullet}$. These calculations are in good agreement with our results (Table 6).

Thus, the ionic radius is not the only parameter to consider. Indeed, the bond length can explain the ranking of H_m (Table 4). Moreover Yashima et al. [81] have calculated Zr-O, and RE-O interatomic distances as a function of the amount of RE_2O_3 in ZrO_2 and compared the results to literature data [97–101]. From all these articles, it was deduced that $r(Y-O)$ decreases when the amount of Y increases, $r(Gd-O)$ increases when the amount of Gd increases and $r(Yb-O)$ stays constant whatever the amount of Yb. As it was previously noted, Yb and Lu are very similar, thus the same behaviour is expected for Lu. Thus, as indicated in the paragraph discussing about the thermal expansion, the following ranking is considered: $r(Y-O) < r(Lu-O) < r(Gd-O)$. The migration enthalpy follows the same order as the thermal expansion, which strengthens the fact that interatomic distances should be preferentially considered to explain H_m changes rather than ionic radius.

Thus, a link between the value of the ionic conductivity and the ionic radius of RE^{3+} and finally with the lattice parameter of the doped fluorite structure can be established. Indeed, increasing the lattice distortion leads to a more difficult migration of oxygen ions. As the ionic radii of Lu^{3+} , Y^{3+} and Gd^{3+} are respectively 0.977 Å, 1.019 Å and 1.053 Å, the most important difference is obtained with Gd^{3+} . Thus, at a fixed temperature and a fixed amount of RE_2O_3 , the forecasted ionic conductivity may be ordered as: $\sigma(Lu_2O_3/HfO_2) > \sigma(Y_2O_3/HfO_2) > \sigma(Gd_2O_3/HfO_2)$. This ranking is checked for RE-14 but not for RE-50 (Figure 10).

In order to explain this behaviour, ionic conductivity measurements as a function of ionic radius for three temperatures (873 K, 1073 K, 1273 K) are reported in the Figure 11. It can be seen that for RE-14, the trend of the ionic conductivity is similar whatever the temperature. Regarding RE-50, the trend of the ionic conductivity is inverted at 873 K, with $\sigma(Lu_2O_3/HfO_2) < \sigma(Y_2O_3/HfO_2) < \sigma(Gd_2O_3/HfO_2)$. This is in good correlation with the evolution of the TECs for 50 mol. % (Figure 6). Indeed, with such high amount of RE_2O_3 , the composition with Lu_2O_3 exhibits a lower TEC than the composition with Y_2O_3 . However, when the temperature increases, the ionic conductivity can be considered as very close for all the RE_2O_3 (Figure 11). Thus, when the amount of RE_2O_3 attains 50 mol %, the ionic conductivity is no more influenced by the ionic radius of RE^{3+} . This is not directly correlated with the activation energies listed in the Table 6 as $H(Lu-50b) > H(Y-50) > H(Gd-50b)$.

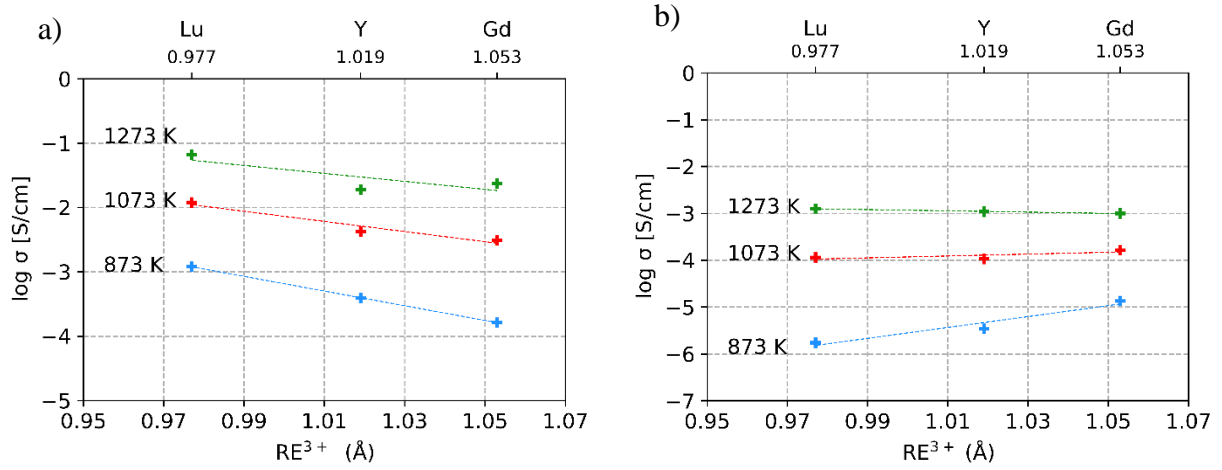


Figure 11 : Ionic conductivity as a function of the ionic radius of RE^{3+} for (a) 14 mol. % and (b) 50 mol. %.

4 CONCLUSIONS

The present study was focused on the development of an ultra-high temperature ceramic coating for satellites combustion chambers. Thus, cubic stabilised hafnia has been selected for its appropriate thermophysical properties and the influence of different amounts and natures of stabilisers for hafnia have been investigated (Y_2O_3 , Gd_2O_3 and Lu_2O_3). These three stabilisers were selected because they allow the conservation of high melting points and because of the different ionic radii of their rare earth cations (0.977 Å, 1.019 Å and 1.053 Å respectively for Lu^{3+} , Y^{3+} and Gd^{3+}). Thus, this have allowed to study the influence of the rare earth ionic radius on the formation of the cubic phase, the thermal expansion and the ionic conductivity of the HfO_2 - RE_2O_3 solid solutions with very high RE_2O_3 amounts (up to 50 mol. %).

Concerning, the stabilisation of the cubic phase, two thermal treatments were assessed in the study at 2023 K under air and 2273 K under argon. Fully formed fluorite $Hf_2RE_2O_7$ phases can be obtained by the solid state reaction at very high temperatures (2273 K). Lowering the sintering temperature to 2023 K induces in some cases the formation of an intermediate phase ($Lu_4Hf_3O_{12}$ in Lu-40b) or the presence of residual precursors (*i.e.* RE_2O_3 in Y-40b, Y50-b and Lu-50b). In the case of materials with Gd_2O_3 , the $Hf_2Gd_2O_7$ phase is fully formed at both temperatures and whatever the amount of rare earth oxide used. However, the pyrochlore superstructure is detected with 40 mol. % of Gd_2O_3 as this composition is close to the pyrochlore domain in the phase diagram. The lattice parameter evolves linearly with the amount of RE_2O_3 in the solid solution and the higher the ionic radius of RE^{3+} cation, the higher the lattice parameter. Moreover, high densification levels (>95% of the theoretical density) are reached whatever the thermal treatment. Grain size is between 13-32 μm for the materials heat treated at 2273 K while it is around 1-7 μm for the samples sintered at 2023 K.

Regarding the thermal expansion coefficients, they were measured between 473 and 1673 K under air. It was observed that the ionic radius of the rare earth cation and its amount influence the lattice parameter, and thus the thermal expansion of the lattice. Indeed, the more the amount of stabiliser, the higher the lattice parameter and the more the amount of oxygen vacancies. This last point modifies the electrostatic interactions in the lattice and influences the thermal expansion. Between, 14 mol. % and 40 mol. % of RE_2O_3 , the thermal expansion coefficient decreases due to lattice contraction around the oxygen vacancies. Then, an increase have been observed for all the stabilisers as RE-O bonds are weaker than Hf-O bonds.

Finally, ionic conductivity was measured for all the compositions. Regarding the influence of the Y_2O_3 amount, an increase leads to a lower ionic conductivity up to 33 mol. %. For higher amounts, the trend of the ionic conductivity is not clear and the activation energies increase slowly. Same trends are observed for Lu_2O_3

and Gd₂O₃-based materials. Comparing RE³⁺ ionic radius, the higher the ionic radius the higher the ionic conductivity. Finally, it should be noted that a very low ionic conductivity was reached with the rhombohedral phase Lu₄Hf₃O₁₂.

Thus, the addition of Lu₂O₃ seems very attractive, and more particularly 40 mol. % of Lu₂O₃ in HfO₂, as it allows to reach, in this study, lower TEC and ionic conductivity compared to Y₂O₃ and Gd₂O₃ stabilisers.

5 ACKNOWLEDGEMENTS

The authors would like to thank Maria Tsoutsouva (ONERA) for X-ray diffraction and Nicolas Horezan and Quentin Barres (ONERA) for the SEM images and EBSD analyses. This work was partially funded by CNES. ICB is supported by the EUR-EIPHI Graduate School (Grant No. 17-EURE-0002).

6 REFERENCES

1. Handy, S. *Applications of Ionic Liquids in Science and Technology*. (BoD – Books on Demand, 2011).
2. Sackheim, R. L. & Masse, R. K. Green Propulsion Advancement: Challenging the Maturity of Monopropellant Hydrazine. *J. Propuls. Power* **30**, 265–276 (2014).
3. Gohardani, A. S. *et al.* Green space propulsion: Opportunities and prospects. *Prog. Aerosp. Sci.* **71**, 128–149 (2014).
4. Pelletier, N. & Lestrade, J.-Y. Overview of the CNES “high performance green monopropellant project”: requirements, organization & breakthroughs. in *Space Propulsion 2018* (2018).
5. Arthur J. Fortini. Combustion Chambers for Advanced Monopropellant Engines | Joint Propulsion Conferences. in (2003). doi:10.2514/6.2003-4730.
6. Upadhyaya, K., Yang, J. M. & Hoffman, W. *Advanced Materials for Ultrahigh Temperature Structural Applications Above 2000 deg C*. <https://apps.dtic.mil/docs/citations/ADA397998> (1997).
7. Sevin, L. Développement de matériaux Ultra-Haute Température: optimisation des propriétés thermomécaniques d’un composite à gradient de propriétés. (PhD thesis from University of Bourgogne Franche-Comté, 2021).
8. Cao, X. Q., Vassen, R. & Stoeber, D. Ceramic materials for thermal barrier coatings. *J. Eur. Ceram. Soc.* **24**, 1–10 (2004).
9. Song, Y. *et al.* Effect of geometric parameter on thermal stress generation in fabrication process of double-ceramic-layers thermal barrier coating system. *J. Eur. Ceram. Soc.* **38**, 3962–3973 (2018).
10. Kulkarni, A. *et al.* Comprehensive microstructural characterization and predictive property modeling of plasma-sprayed zirconia coatings. *Acta Mater.* **51**, 2457–2475 (2003).
11. Vaßen, R., Jarligo, M. O., Steinke, T., Mack, D. E. & Stöver, D. Overview on advanced thermal barrier coatings. *Surf. Coat. Technol.* **205**, 938–942 (2010).
12. Zhao, Y. *et al.* Thermal Aging Behavior of Axial Suspension Plasma-Sprayed Yttria-Stabilized Zirconia (YSZ) Thermal Barrier Coatings. *J. Therm. Spray Technol.* **24**, 338–347 (2015).
13. Bakan, E. & Vaßen, R. Ceramic Top Coats of Plasma-Sprayed Thermal Barrier Coatings: Materials, Processes, and Properties. *J. Therm. Spray Technol.* **26**, 992–1010 (2017).
14. Clarke, D. R. & Phillpot, S. R. Thermal barrier coating materials. *Mater. Today* **8**, 22–29 (2005).
15. Saruhan, B., Francois, P., Fritscher, K. & Schulz, U. EB-PVD processing of pyrochlore-structured La₂Zr₂O₇-based TBCs. *Surf. Coat. Technol.* **182**, 175–183 (2004).

16. Vaßen, R., Traeger, F. & Stöver, D. New Thermal Barrier Coatings Based on Pyrochlore/YSZ Double-Layer Systems. *Int. J. Appl. Ceram. Technol.* **1**, 351–361 (2004).
17. Fergus, J. W. Zirconia and Pyrochlore Oxides for Thermal Barrier Coatings in Gas Turbine Engines. *Metall. Mater. Trans. E* **1**, 118–131 (2014).
18. Alvin, M. A. *et al.* Extreme Temperature Coatings for Future Gas Turbine Engines. in (American Society of Mechanical Engineers Digital Collection, 2013). doi:10.1115/GT2013-94432.
19. Poerschke, Jackson & Levi. Silicate Deposit Degradation of Engineered Coatings in Gas Turbines: Progress Toward Models and Materials Solutions. *Annu. Rev. Mater. Res.* **47**, 297–330 (2017).
20. Schulz, U., Nowotnik, A., Kunkel, S. & Reiter, G. Effect of processing and interface on the durability of single and bilayer 7YSZ / gadolinium zirconate EB-PVD thermal barrier coatings. *Surf. Coat. Technol.* **381**, (2020).
21. Gomez Chavez, J. J. *et al.* Effects of yttria content on the CMAS infiltration resistance of yttria stabilized thermal barrier coatings system. *J. Mater. Sci. Technol.* **43**, 74–83 (2020).
22. Andrievskaya, E. R. Phase equilibria in the refractory oxide systems of zirconia, hafnia and yttria with rare-earth oxides. *J. Eur. Ceram. Soc.* **28**, 2363–2388 (2008).
23. Mahade, S., Curry, N., Björklund, S., Markocsan, N. & Nylén, P. Failure analysis of Gd₂Zr₂O₇/YSZ multi-layered thermal barrier coatings subjected to thermal cyclic fatigue. *J. Alloys Compd.* **689**, 1011–1019 (2016).
24. Ruud, J. A., Bartz, A., Borom, M. P. & Johnson, C. A. Strength Degradation and Failure Mechanisms of Electron-Beam Physical-Vapor-Deposited Thermal Barrier Coatings. *J. Am. Ceram. Soc.* **84**, 1545–1552 (2001).
25. Zhu, D. *Hafnia-Based Materials Developed for Advanced Thermal/Environmental Barrier Coating Applications*. <https://ntrs.nasa.gov/search.jsp?R=20050192261> (2004).
26. Haggerty, R. P., Sarin, P., Apostolov, Z. D., Driemeyer, P. E. & Kriven, W. M. Thermal Expansion of HfO₂ and ZrO₂. *J. Am. Ceram. Soc.* **97**, 2213–2222 (2014).
27. Stecura, S., Campbell, W. J., United States & Bureau of Mines. *Thermal expansion and phase inversion of rare-earth oxides*. (U.S. Department of the Interior, Bureau of Mines, 1961).
28. Zhu, D. *et al.* *Advanced Environmental Barrier Coating Development for SiC-SiC Ceramic Matrix Composite Components*. <https://ntrs.nasa.gov/search.jsp?R=20170009570> (2017).
29. Hu, W., Lei, Y., Zhang, J. & Wang, J. Mechanical and thermal properties of RE₄Hf₃O₁₂ (RE=Ho, Er, Tm) ceramics with defect fluorite structure. *J Mater. Sci.* **35**, 2064–2069 (2019).
30. Lakiza, S. M. *et al.* The Role of Hafnium in Modern Thermal Barrier Coatings. *Powder Metall. Met. Ceram.* **60**, 78–89 (2021).
31. Poerschke, D. L. & Levi, C. G. Effects of cation substitution and temperature on the interaction between thermal barrier oxides and molten CMAS. *J. Eur. Ceram. Soc.* **35**, 681–691 (2015).
32. Zhu, D., Bansal, N. P. & Miller, R. A. Thermal Conductivity and Stability of HfO₂-Y₂O₃ and La₂Zr₂O₇ Evaluated for 1650°C Thermal/Environmental Barrier Coating Applications. in *Ceramic Transactions Series* (eds. Bansal, N. P., Singh, J. P., Kriven, W. M. & Schneider, H.) 329–343 (John Wiley & Sons, Inc., 2012). doi:10.1002/9781118406892.ch23.
33. Buckley, J. D. W. *Effects of Cyclic Heating and Thermal Shock on Hafnia Stabilized with Calcia, Magnesia, and Yttria*. <https://ntrs.nasa.gov/search.jsp?R=19690025169> (1969).
34. Trubelja, M. F. & Stubican, V. S. Ionic Conductivity of the Fluorite-Type Hafnia-R₂O₃ Solid Solutions. *J. Am. Ceram. Soc.* **74**, 2489–2494 (1991).
35. Luo, X., Zhou, W., Ushakov, S. V., Navrotsky, A. & Demkov, A. A. Monoclinic to tetragonal transformations in hafnia and zirconia: A combined calorimetric and density functional study. *Phys. Rev. B* **80**, 134119 (2009).
36. Stacy, D. W. & Wilder, D. R. The Yttria-Hafnia System. *J. Am. Ceram. Soc.* **58**, 285–288 (1975).

37. Wang, J., Li, H. P. & Stevens, R. Hafnia and hafnia-toughened ceramics. *J. Mater. Sci.* **27**, 5397–5430 (1992).
38. Hudak, B. M. *et al.* Real-time atomistic observation of structural phase transformations in individual hafnia nanorods. *Nat. Commun.* **8**, 1–9 (2017).
39. Bocanegra-Bernal, M. H. & Diaz, S. Phase transitions in zirconium dioxide and related materials for high performance engineering ceramics. *J Mater. Sci.* **37**, 4947–4971 (2002).
40. Zhu, D. & Miller, R. A. Sintering and creep behavior of plasma-sprayed zirconia and hafnia-based thermal barrier coatings. *Surf. Coat. Technol.* **108–109**, 114–120 (1998).
41. Duran, P. & Pascual, C. Phase equilibria and ordering in the system $\text{HfO}_2\text{-Yb}_2\text{O}_3$. *J. Mater. Sci.* **19**, 1178–1184 (1984).
42. Hayashi, H. *et al.* Thermal expansion coefficient of yttria stabilized zirconia for various yttria contents. *Solid State Ion.* **176**, 613–619 (2005).
43. Hayashi, H. *et al.* Thermal expansion of Gd-doped ceria and reduced ceria. *Solid State Ion.* **132**, 227–233 (2000).
44. Marrocchelli, D., Bishop, S. R. & Kilner, J. Chemical expansion and its dependence on the host cation radius. *J. Mater. Chem. A* **1**, 7673–7680 (2013).
45. Yadav, K. K. *et al.* Low temperature synthesis process of stabilization of cubic yttria stabilized zirconia spindles: an important high temperature ceramic material. *Mater. Res. Express* **4**, 105044 (2017).
46. Rodaev, V. V., Razlivalova, S. S., Tyurin, A. I., Zhigachev, A. O. & Golovin, Y. I. Microstructure and Phase Composition of Yttria-Stabilized Zirconia Nanofibers Prepared by High-Temperature Calcination of Electrospun Zirconium Acetylacetonate/Yttrium Nitrate/Polyacrylonitrile Fibers. *Fibers* **7**, 82 (2019).
47. Kulkarni, A. *et al.* Comprehensive microstructural characterization and predictive property modeling of plasma-sprayed zirconia coatings. *Acta Mater.* **51**, 2457–2475 (2003).
48. Zhao, Y. *et al.* Thermal Aging Behavior of Axial Suspension Plasma-Sprayed Yttria-Stabilized Zirconia (YSZ) Thermal Barrier Coatings. *J. Therm. Spray Technol.* **24**, 338–347 (2015).
49. Fu-kang, F., Kuznetsov, A. K. & Keler, É. K. Phase relationships in the system $\text{Y}_2\text{O}_3\text{-ZrO}_2$. *Bull. Acad. Sci. USSR Div. Chem. Sci.* **12**, 542–549 (1963).
50. Fonseca, F. Analysis of the formation of $\text{ZrO}_2\text{:Y}_2\text{O}_3$ solid solution by the electrochemical impedance spectroscopy technique. *Solid State Ion.* **149**, 309–318 (2002).
51. Li, C., Ren, C., Ma, Y., He, J. & Guo, H. Effects of rare earth oxides on microstructures and thermo-physical properties of hafnia ceramics. *J Mater. Sci. Technol.* **72**, 144–153 (2021).
52. Simoncic, P. & Navrotsky, A. Energetics of rare-earth-doped hafnia. *J. Mater. Res.* **22**, 876–885 (2007).
53. Yokoyama, M., Ota, T. & Yamai, I. Flux growth of rare-earth stabilized zirconia and hafnia crystals. *J. Cryst. Growth* **94**, 287–292 (1989).
54. Ramana, C. V., Noor-A-Alam, M., Gengler, J. J. & Jones, J. G. Growth, Structure, and Thermal Conductivity of Yttria-Stabilized Hafnia Thin Films. *ACS Appl. Mater. Interfaces* **4**, 200–204 (2012).
55. Zhou, W., Ushakov, S. V. & Navrotsky, A. Yttria-stabilized hafnia: Thermochemistry of formation and hydration of nanoparticles. *J. Mater. Res.* **27**, 1022–1028 (2012).
56. Winter, M. R. & Clarke, D. R. Thermal conductivity of yttria-stabilized zirconia–hafnia solid solutions. *Acta Mater.* **54**, 5051–5059 (2006).
57. Gibson, I. R., Dransfield, G. P. & Irvine, J. T. S. Sinterability of commercial 8 mol% yttria-stabilized zirconia powders and the effect of sintered density on the ionic conductivity. *J. Mater. Sci.* **33**, 4297–4305 (1998).
58. Manning, P. S., Sirman, J. D., De Souza, R. A. & Kilner, J. A. The kinetics of oxygen transport in 9.5 mol % single crystal yttria stabilised zirconia. *Solid State Ion.* **100**, 1–10 (1997).
59. Weyl, A. & Janke, D. High-Temperature Ionic Conduction in Multicomponent Solid Oxide Solutions Based on HfO_2 . *J. Am. Ceram. Soc.* **79**, 2145–2155 (1996).

60. Sévin, L. *et al.* Effect of high-content Ytria on the thermal expansion behaviour and ionic conductivity of a stabilised cubic Hafnia. *J. Eur. Ceram. Soc.* **40**, 5859–5869 (2020).
61. Sévin, L. *et al.* Structural Stability of Hafnia-Based Materials at Ultra-High Temperature. *Materials Science Forum* <https://www.scientific.net/MSF.941.1972> (2018) doi:10.4028/www.scientific.net/MSF.941.1972.
62. Šály, V., Hartmanová, M. & Glushková, V. B. Electrical behaviour of HfO₂ stabilized with rare earths. *Solid State Ion.* **36**, 189–192 (1989).
63. Hartmanová, M., Hanic, F., Putyera, K., Tunega, D. & Glushkova, V. B. Structure and physical properties of stabilized HfO₂-R₂O₃ (R = Sc, Yb, Y, Tb, Gd, Er). *Mater. Chem. Phys.* **34**, 175–180 (1993).
64. Kim, D.-J. Lattice Parameters, Ionic Conductivities, and Solubility Limits in Fluorite-Structure MO₂ Oxide [M = Hf⁴⁺, Zr⁴⁺, Ce⁴⁺, Th⁴⁺, U⁴⁺] Solid Solutions. *J. Am. Ceram. Soc.* **72**, 1415–1421 (1989).
65. Mogensen, M., Lybye, D., Bonanos, N., Hendriksen, P. V. & Poulsen, F. W. Factors controlling the oxide ion conductivity of fluorite and perovskite structured oxides. *Solid State Ion.* **174**, 279–286 (2004).
66. Caglioti, G., Paoletti, A. & Ricci, F. P. Choice of collimators for a crystal spectrometer for neutron diffraction. *Nucl. Instrum.* **3**, 223–228 (1958).
67. Toraya, H. A new method for quantitative phase analysis: Direct derivation of weight fractions from observed intensities and chemical composition data of individual crystalline phases. *Rigaku J.* **34**, 3–8 (2018).
68. Karthik, C., Anderson, T. J., Gout, D. & Ubig, R. Transmission electron microscopic study of pyrochlore to defect-fluorite transition in rare-earth pyrohafnates. *J. Solid State Chem.* **194**, 168–172 (2012).
69. Subramanian, M. A., Aravamudan, G. & Subba Rao, G. V. Oxide pyrochlores — A review. *Prog. Solid State Chem.* **15**, 55–143 (1983).
70. Popov, V. V. *et al.* Fluorite-pyrochlore phase transition in nanostructured Ln₂Hf₂O₇ (Ln = La-Lu). *J. Alloys Compd.* **689**, 669–679 (2016).
71. Rushton, M. J. D., Grimes, R. W., Stanek, C. R. & Owens, S. Predicted pyrochlore to fluorite disorder temperature for A₂Zr₂O₇ compositions. *J. Mater. Res.* **19**, 1603–1604 (2004).
72. Ushakov, S. V., Navrotsky, A., Tangeman, J. A. & Helean, K. B. Energetics of defect fluorite and pyrochlore phases in lanthanum and gadolinium hafnates. *J. Am. Ceram. Soc.* **90**, 1171–1176 (2007).
73. Trubelja, M. F. & Stubican, V. S. Ionic Conductivity of the Fluorite-Type Hafnia-R₂O₃ Solid Solutions. *J. Am. Ceram. Soc.* **74**, 2489–2494 (1991).
74. Yashima, M., Ishizawa, N. & Yoshimura, M. Application of an Ion-Packing Model Based on Defect Clusters to Zirconia Solid Solutions: II, Applicability of Vegard's Law. *J. Am. Ceram. Soc.* **75**, 1550–1557 (1992).
75. Stacy, D. W. & Wilder, D. R. The Ytria-Hafnia System. *J. Am. Ceram. Soc.* **58**, 285–288 (1975).
76. Ingel, R. P. & Iii, D. L. Lattice Parameters and Density for Y₂O₃-Stabilized ZrO₂. *J. Am. Ceram. Soc.* **69**, 325–332 (1986).
77. Marrocchelli, D., Bishop, S. R., Tuller, H. L. & Yildiz, B. Understanding Chemical Expansion in Non-Stoichiometric Oxides: Ceria and Zirconia Case Studies. *Adv. Funct. Mater.* **22**, 1958–1965 (2012).
78. Sameshima, S., Kawaminami, M. & Hirata, Y. Thermal Expansion of Rare-Earth-Doped Ceria Ceramics. *J. Ceram. Soc. Jpn.* **110**, 597–600 (2002).
79. Li, C. *et al.* Effect of Y doping on microstructure and thermophysical properties of yttria stabilized hafnia ceramics. *Ceram. Int.* **44**, 18213–18221 (2018).
80. Meyer, M., Nicoloso, N. & Jaenisch, V. Percolation model for the anomalous conductivity of fluorite-related oxides. *Phys. Rev. B* **56**, 5961–5966 (1997).
81. Yashima, M., Ishizawa, N. & Yoshimura, M. Application of an Ion-Packing Model Based on Defect Clusters to Zirconia Solid Solutions: I, Modeling and Local Structure of Solid Solutions. *J. Am. Ceram. Soc.* **75**, 1541–1549 (1992).

82. Hongsong, Z., Lei, S., Yongde, Z., Gang, L. & Zhenjun, L. Thermal Conductivities and Thermal Expansion Coefficients of $(\text{Sm}_{0.5}\text{Gd}_{0.5})_2(\text{Ce}_{1-x}\text{Zr}_x)_2\text{O}_7$ Ceramics. *J. Mater. Eng. Perform.* **24**, 3394–3399 (2015).
83. Lehmann, H., Pitzer, D., Pracht, G., Vassen, R. & Stöver, D. Thermal Conductivity and Thermal Expansion Coefficients of the Lanthanum Rare-Earth-Element Zirconate System. *J. Am. Ceram. Soc.* **86**, 1338–1344 (2003).
84. Pavlik, A., Ushakov, S. V., Navrotsky, A., Benmore, C. J. & Weber, R. J. K. Structure and thermal expansion of Lu_2O_3 and Yb_2O_3 up to the melting points. *J. Nucl. Mater.* **495**, 385–391 (2017).
85. Arnal, S., Fourcade, S., Mauvy, F. & Rebillat, F. Design of a new yttrium silicate Environmental Barrier Coating (EBC) based on the relationship between microstructure, transport properties and protection efficiency. *J. Eur. Ceram. Soc.* **42**, 1061–1076 (2022).
86. Kobayashi, K. & Sakka, Y. Rudimental research progress of rare-earth silicate oxyapatites: their identification as a new compound until discovery of their oxygen ion conductivity. *J. Ceram. Soc. Jpn.* **122**, 649–663 (2014).
87. Marrero-López, D., dos Santos-Gómez, L., León-Reina, L., Canales-Vázquez, J. & Losilla, E. R. Influence of the microstructure on the bulk and grain boundary conductivity in apatite-type electrolytes. *J. Power Sources* **245**, 107–118 (2014).
88. Kharton, V. V., Naumovich, E. N. & Vecher, A. A. Research on the electrochemistry of oxygen ion conductors in the former Soviet Union. I. ZrO_2 -based ceramic materials. *J. Solid State Electrochem.* **3**, 61–81 (1999).
89. Stortelder, J. K. Ionic Conductivity in Ytria-Stabilized Zirconia Thin Films grown by Pulsed Laser Deposition. 47.
90. Zhang, C. *et al.* Ionic conductivity and its temperature dependence of atmospheric plasma-sprayed yttria stabilized zirconia electrolyte. *Mater. Sci. Eng. B* **137**, 24–30 (2007).
91. Pietrucci, F., Bernasconi, M., Laio, A. & Parrinello, M. Vacancy-vacancy interaction and oxygen diffusion in stabilized cubic ZrO_2 from first principles. *Phys. Rev. B* **78**, 094301 (2008).
92. Zhang, W., Chen, W.-Z., Sun, J.-Y. & Jiang, Z.-Y. Theoretical prediction of ion conductivity in solid state HfO_2 . *Chin. Phys. B* **22**, 016601 (2013).
93. Pornprasertsuk, R., Ramanarayanan, P., Musgrave, C. B. & Prinz, F. B. Predicting ionic conductivity of solid oxide fuel cell electrolyte from first principles. *J. Appl. Phys.* **98**, 103513 (2005).
94. Kim, D.-J. Lattice Parameters, Ionic Conductivities, and Solubility Limits in Fluorite-Structure MO_2 Oxide [$\text{M} = \text{Hf}^{4+}, \text{Zr}^{4+}, \text{Ce}^{4+}, \text{Th}^{4+}, \text{U}^{4+}$] Solid Solutions. *J. Am. Ceram. Soc.* **72**, 1415–1421 (1989).
95. Arachi, Y., Sakai, H., Yamamoto, O., Takeda, Y. & Imanishai, N. Electrical conductivity of the ZrO_2 – Ln_2O_3 (Ln =lanthanides) system. *Solid State Ion.* **121**, 133–139 (1999).
96. Butler, V., Catlow, C. R. A. & Fender, B. E. F. The defect structure of anion deficient ZrO_2 . *Solid State Ion.* **5**, 539–542 (1981).
97. Veal, B. W., McKale, A. G., Paulikas, A. P., Rothman, S. J. & Nowicki, L. J. EXAFS study of yttria stabilized cubic zirconia. *Phys. BC* **150**, 234–240 (1988).
98. Tuilier, M. H., Dexpert-Ghys, J., Dexpert, H. & Lagarde, P. X-ray absorption study of the ZrO_2 – Y_2O_3 system. *J. Solid State Chem.* **69**, 153–161 (1987).
99. Goldman, A. I., Canova, E., Kao, Y. H., Roth, W. L. & Wong, R. EXAFS Studies of Ytria Stabilized Zirconia. in *EXAFS and Near Edge Structure III* (eds. Hodgson, K. O., Hedman, B. & Penner-Hahn, J. E.) 442–444 (Springer, 1984). doi:10.1007/978-3-642-46522-2_113.
100. Morikawa, H. *et al.* Local Structures Around Y Atoms in Y_2O_3 -Stabilized Tetragonal ZrO_2 . *J. Ceram. Soc. Jpn.* **96**, 253–258 (1988).
101. Uehara, T., Koto, K., Emura, S. & Kanamaru, F. Exafs study of the fluorite and pyrochlore compounds in the system ZrO_2 - Gd_2O_3 . *Solid State Ion.* **23**, 331–337 (1987).